Potassium silicate alteration in porphyry copper-gold deposits: a case study at the giant maar-diatreme hosted Grasberg deposit, Indonesia

Richard W. Henley[1]
Terrence Mernagh[2]
Clyde Leys[3]
Ulrich Troitzsch[1]
Joseph Bevitt[4]
Frank Brink[5]
Joe Gardner[6]
Lydia Knuefing[1]
John Wheeler[6]
Limaye, Ajay[1]
Michael Turner[1]
Yulai Zhang[1]

1. ARC Training Centre for M3D Innovation, Research School of Physics, Australian National University, Canberra, ACT, Australia
2. Research School of Earth Sciences, The Australian National University, Canberra, ACT 0200, Australia
3. P.T. Freeport Indonesia, Tembagapura, Papua, Indonesia
4. Australian Nuclear Science and Technology Organisation, Lucas Heights, NSW 2234, Australia
5. Centre for Advanced Microscopy, The Australian National University, ACT 0200, Australia
6. Department of Earth, Ocean, and Ecological Sciences, University of Liverpool, Liverpool, U.K.

Abstract

Potassium silicate alteration is a hallmark of the porphyry copper deposits that supply two thirds of the world's annual copper demand. These deposits formed in the cores of calc-alkaline to alkaline volcanic systems from the flux of magmatic gas that transported copper and other metals from source to the surface. The giant 3.2 Ma Grasberg Cu-Au deposit formed within a maar-diatreme complex following a resurgence in magmatism. The defined resources of this deposit occur from a few hundred metres depth to 1.7 kilometres below the paleosurface which, uniquely in this deposit, is partially preserved as a section of maar tuffs.

Potassium silicate alteration has commonly been interpreted as being the result of the addition of potassium to the porphyry copper host rocks via pervasive interaction with a large volume of a potassium-rich brine that is commonly presumed to be of magmatic origin. However, the data reported here show that alteration at the deposit scale is essentially isochemical with respect to the major rock-forming components and that only sulphur and the

economic metals (Cu, Mo, Au, etc.) are added by flux of reactive magmatic gas containing SO_2 and HCl from source intrusions at depth. Silicate solubilities are very low so that only a minor fraction of the total alkalis in the host rock are extracted by alteration reactions and then discharged at the paleo-surface. Reaction of the magmatic gas phase with plagioclase results in the coupled deposition of anhydrite ($CaSO_4$) and disproportionation of SO_2 to release H_2S. The in-situ release of H_2S immediately scavenges Cu and other chalcophile metals from the continuing magmatic gas flux to form the Cu-, Fe- and other sulphides that, in sufficient concentration, make up the economic reserve available to mining.

The sequestration of Ca into anhydrite, along with deposition of silica into early quartz veins, increases the concentration of the other major components (K_2O, Na_2O, MgO, etc) in the remaining silicate assemblage within the porous host rock. The result is the development of intermingled potassium-enriched silicate and sulphur-rich (anhydrite-sulphide) sub-assemblages that constitute the mineralized phyllic or potassic alteration zones. These crystallize according to their pressure and depth into alteration assemblages dominated by potassic phyllosilicates, quartz and pyrite in the phyllic alteration zone, and alkali feldspar and phlogopitic-biotite plus minor andalusite and corundum in the central potassic zone. Dissolution and recrystallization of primary magmatic biotite in the host rock releases K as well as Fe, the latter (along with amphibole and feldspar) providing iron for the formation of chalcopyrite, bornite and pyrite. The in-situ release of H_2S through anhydrite formation, immediately scavenges Cu and other chalcophile metals from the continuing magmatic gas flux to form the Cu-Fe- and other sulphides that, in sufficient concentration, make up the economic reserve available to mining. Understanding of the alteration processes during porphyry copper formation also provides insights into gas-solid reactions processes inside active magmatic arc volcanoes but the magnitude of copper mineralisation is dependent on the original metal content of the source of the magmatic gas phase.

Key words

Porphyry copper; alteration; feldspar replacement; microporosity.

Highlights

- Potassium silicate alteration is commonly assumed to be due to potassium addition
- New analytical data from Grasberg show that alteration was quasi-isochemical
- Apparent potassium enrichment is due to sequestration of Ca into anhydrite
- Anhydrite formation releases H_2S from SO_2 with co-deposition of sulphides
- There is no potassic brine addition during porphyry copper formation

1. Introduction

More than two thirds of the annual global production of copper (Singer, 2017) comes from 'porphyry copper' deposits – the very large hydrothermal ore deposits that formed inside the cores of volcanic systems that were active in magmatic arcs throughout the Phanerozoic (Henley and Berger, 2013; Henley and Ellis, 1983; Sillitoe, 1973; Sillitoe, 2010). A defining geochemical characteristic of these deposits is the association of economic grades of sulphide mineralisation (presently averaging > ~ 0.5 % copper) with pervasive *potassium silicate* rock alteration (Meyer and Hemley, 1967; Sillitoe, 2010). Potassium silicate alteration was initially defined for porphyry copper deposits by Creasey (1959) as characterized by the presence of secondary potassium feldspar and micas within altered rocks. Further observations were provided by Meyer and Hemley (1967). Recognition of the consistency of alteration zonation within many well-studied deposits worldwide has since led to sub-division of potassium silicate alteration assemblages into *'potassic'* assemblages dominated by potassium feldspar (often with abundant albite - Meyer and Hemley (1967)) and phlogopitic biotite, and phyllic (syn. sericitic) assemblages characterized by fine-grained potassic 'white' mica (or illite/muscovite mixed layer micas) and quartz.

Potassium silicate alteration has generally been assumed to be the result of infiltration of exotic hypersaline *liquid-phase* brines, directly from intrusives (Frank and Vaccaro, 2012; Meyer and Hemley, 1967; Paterson and Cloos., 2005b; Sillitoe, 2010). More recently, Lerchbaumer and Audétat (2012) showed that the vapour to brine mass ratio at Alumbrera was 4 to 9, which translates to a volume proportion of 96 to 98% vapour. An analogous conclusion for the Grasberg deposit was reached by Mernagh et al. (2020) based on enthalpy constraints (i.e., ~98 vol% vapour). Similarly, other researchers have proposed that potassic alteration is mineralisthe product of high temperature *gas-solid* reactions within the sub-volcanic environment of porphyry copper formation (Henley et al., 2015; Henley and Seward, 2018; Mernagh et al., 2020; Nadeau et al., 2016) with the *gas phase* composition equivalent to that of high temperature gas mixtures released by fumaroles in modern volcanoes. These gas mixtures are dominated by H_2O, SO_2, H_2S, HCl and HF and have very low concentrations of alkali metals (Henley and Seward, 2018) of less than 0.1 wt% and commensurate, as discussed elsewhere (Mernagh et al., 2020) with the composition of vapour-rich inclusions from porphyry copper deposits.

The above observations then raise a paradox of how such large-scale potassium enrichment develops throughout alteration and mineralisation during the formation of porphyry copper-gold deposits worldwide without the addition of high salinity brines. In this paper we address this paradox through analysis of micro to mine scale petrographic and geochemical data using a range of techniques including high resolution tomography to determine microporosity. The study is based on samples from the giant Grasberg porphyry copper-gold deposit (Indonesia, longitude 137.1144°, latitude −4.0461°) whose metal content is over 32 Mt of Cu (Leys et al., 2012).

1. Geological context

The Grasberg deposit is one of the youngest and most comprehensively studied porphyry deposits in the world (Leys et al., 2020; Leys et al., 2012). It is one of a group of major porphyry

and related-skarn deposits, including the giant Ertsberg deposit (Figure 1), within the Grasberg-Ertsberg mining district of Papua, Indonesia (Leys et al., 2020; Leys et al., 2012; MacDonald and Arnold, 1994). The deposit formed in the second of two porphyry mineralising events (Leys et al., 2020), an earlier Cu-Mo event that postdated the ~3.4-3.3 Ma Gajah Tidur intrusion and a later Cu-Au event that followed the emplacement of the 3.22 + 0.05 Ma Main Grasberg Intrusion. Both events deposited mineralisation within the upper 2 to 3 km of a maar-diatreme volcanic complex as a result of magmatic vapour release from underlying intrusions whose final, post-mineralisation activity is preserved as a suite of monzodiorite dykes dated at 3.09 $\pm$ 0.05 Ma. The Grasberg deposit itself is defined by the distribution of the dominant alteration minerals (anhydrite, K-feldspar, muscovite and pyrite). A vertically extensive, cylindrical column of high-grade copper-gold mineralisation is closely related with bornite in the centre of the deposit (Figure 2) associated with the Main Grasberg Intrusion (Figure 3) as is detailed below (Leys et al., 2020). Sub-grade mineralisation has been defined to 2500m elevation (1700 metres below the paleosurface), and the very limited drilling below this to 2200 m elevation (2km below the paleosurface) has identified patchy, low-grade mineralisation.

Uniquely, the Grasberg porphyry copper-gold deposit retains clear evidence of its volcanic setting and depth of formation. The Grasberg deposit comprises about 2 km^3 of altered rock material and is centered within a diatreme that formed during the partly-eruptive, early 3.6-3.3 Ma Dalam stage of the Grasberg Igneous Complex which intruded a sequence of Mesozoic carbonate and siliclastic rocks. The Cu-Au mineralisation occurs principally through the Dalam Fragmental Andesite breccia that infills the vent of the previously eruptive diatreme. Dalam igneous units are the principal host of mineralisation in the Grasberg deposit (Figure 3a), with their Cu-Au grades highest adjacent to their contact with the Main Grasberg intrusion. The unaltered primary compositions of the Dalam volcanic and intrusive rocks are partially obscured by the spatial extent of low-grade metamorphism of the volcanic sequence across the district and weak, more localised hydrothermal alteration related to the two subsequent porphyry mineralising events (Leys et al., 2020; MacDonald and Arnold, 1994). However retention of primary igneous textures and calcic plagioclase, as well as sample location with respect to the deposit, enable definition of the petrochemical affinity of the primary igneous rocks. Average whole rock analyses for 1400 outcrop and drillhole samples of Dalam intrusive and volcanic rocks were reported by MacDonald and Arnold (1994). These data provide a relative measure of the extent of alteration from their sulphur content (representing anhydrite and sulphides) and their loss on ignition results (representing loss of water from deuteric and phyllic alteration minerals that replaced primary potassium silicates and loss of CO_2 from minor carbonate alteration). Table 1 recasts these data by converting Fe_2O_3 to FeO, normalising on a LOI and S-free basis and ignoring the minor contribution of introduced transition metals (e.g. Cu, Mo). Recast in this way, the primary Dalam units previously reported as ‘monzodiorites’ and related ‘andesitic’ volcanics may be reclassified as high-K tholeiitic rocks (Arculus, 2003; Zimmer et al., 2010).

Detailed petrographic descriptions of the least-altered Dalam intrusive rocks and their volcanic equivalents are provided by Pollard and Taylor (2002) and by Paterson (2004). Both report that Dalam samples are petrographically and mineralogically highly variable. They generally contain between 20 and 45 vol.% plagioclase phenocrysts, but in many samples the plagioclase phenocrysts have been completely destroyed by alteration. Some rare primary Dalam plagioclase phenocrysts are recorded as having oscillatory zoning ranging from An_{25} to An_{50} (Paterson, 2004), some of which were broken as indicated by their truncated zoning. Dalam units also contain 5 to 25 vol.% of primary magmatic biotite phenocrysts but in many altered samples this is progressively replaced by more phlogopitic biotite. Primary magmatic biotite

phenocrysts are distinguished from secondary biotite by their preserved euhedral to subhedral shape, their high Ti with respect to Mg numbers (Mg# = Mg/(Mg+Fe) from about 55 to 75) and their relative K and Si ratios with respect to Al (Paterson, 2004). Rare primary igneous hornblende is also recorded (Paterson (2004) but was not identified in our samples. The groundmass of Dalam units comprises potassic feldspar, plagioclase and quartz (~2:1 K-feldspar to quartz) and makes up ~40 vol.% of the rock. Interestingly, Paterson and Cloos (2005a) also noted that the fine- to medium-grained groundmass of the Dalam Fragmental volcanics may have been glassy and reported the rare presence of albite (see discussion below). In addition, MacDonald and Arnold (1994) noted the presence of 1-2 wt% igneous magnetite in all Grasberg district igneous rocks that they examined.

The spatial extent and geometry of alteration zones at Grasberg are provided by Leys et al. (2020) and are shown in cross-section (Figure 3b) based on more than 4000 X-ray Diffraction (XRD) and petrographic analyses obtained from intensive in-mine drilling. These data clearly show the concentrations of biotite, K-feldspar and anhydrite as a central vertical core (green colours in Figure 3b) surrounded by a phyllic alteration annulus (yellow-orange in Figure *3*b), and the wider distribution of Cu as both disseminated and vein-hosted chalcopyrite and bornite, extending outward from the core across both of these alteration zones. A narrow zone of more massive sulphide, known as the Heavy Sulphde Zone (HSZ), forms a distinctive assemblage at the contact of the diatreme vent with surrounding sediments as shown in Figure 3b. The overall pattern of zonation at Grasberg is very similar to that commonly observed in porphyry copper deposits around the world (Burnham, 1962; Lowell and Guilbert, 1970). At Grasberg, the central core alteration facies (that is cut through by the later Kali dykes) is defined by the assemblage orthoclase-quartz-anhydrite with secondary magnetite present in the upper ~1000 m (within the fragmental sub-volcanic units that infill the upper part of the diatreme) but are absent in the underlying porphyritic intrusions. Surrounding this core is an annulus of quartz-'sericite'-anhydrite-pyrite (*phyllic)* alteration that may be further sub-divided according to relative abundance of quartz and 'sericite'. Sericite is a generic term for crystalline potassic phyllosilicates (micas) in altered rocks within the phyllic zone and includes smectite/illite, illite, illite/muscovite and muscovite series minerals. Other significant minerals present within the potassic and phyllic alteration zones include secondary apatite and hornblende (Paterson, 2004), the former as both disseminated grains and in veins. Andalusite, diaspore and corundum (Penniston-Dorland, 1997), occur in the core of the Grasberg potassic alteration in association with hydrothermal biotite (Paterson, 2004; Penniston-Dorland, 1997), as they do in a number of other porphyry copper deposits.

The volumes of each alteration assemblage within the Grasberg deposit and the proportions (Wt%) of their major mineral phases are summarized in Table 2, based on an extensive program of diamond core drilling and representative XRD analyses (Freeport-McMoran proprietary data) between 2400 and 3800 meters above sea level (masl). A total of 2906 samples were analysed from the potassium feldspar ('potassic') alteration zone and 824 from the surrounding phyllic zone (Figure 2). Models based on these results show that the volume of the potassic alteration zone is 1.05 km^3 and the phyllic zone is 1.17 km^3. The XRD results for the proportions of K-feldspar, phlogopitic biotite and muscovite shown in Table 2 clearly distinguish these two alteration assemblages and highlight the higher copper grade of the potassium feldspar zone. This higher-grade potassic core contains 7.7 Wt% of combined anhydrite and gypsum and the phyllic zone contains 3.6 Wt%. The phyllic zone is distinguished also by its very high average pyrite content (14 Wt%) relative to the potassic zone (2 Wt%).

2. Sampling and Analytical Methods

Earlier studies of porphyry copper alteration were based on detailed field observations supported by XRD, electron microprobe analyzes and optical microscopy that in this study we have complemented with high resolution SEM mineral mapping and X-ray and thermal neutron micro-computed tomography (μCT). This approach provides detailed spatial understanding of mineral relationships and of the distribution of microporosity the latter crucial to consideration of mineral replacement processes. The data analysis provided here is fundamentally underpinned by the extensive and highly detailed petrographic descriptions for Grasberg provided by Penniston-Dorland (1997), Pollard and Taylor (2002) and Paterson (2004) of samples obtained during earlier investigations.

2.1 Samples

The samples described here were selected to first compare and contrast the assemblages within weak to intense stages of potassium silicate alteration and second to attempt to unravel the chemical mechanisms that control these alteration reactions and their accompanying mineralisation. Two potassium silicate altered samples of Dalam volcanics were selected from underground drill holes for comparative analysis and their locations are shown in Figure 3a and b. Sample GP was collected as a loose block from within the open pit at ~1000 m higher elevation and is illustrative of the intense phyllic alteration that surrounds the potassic core of the deposit. Entire samples and sub-cores taken from them were examined using X-ray μCT, followed by high resolution EDS mineral mapping, XRD and a range of standard petrographic techniques based on polished and thin sections that were prepared using water-free polishing paste to avoid removal of anhydrite.

Alteration mineralogy and whole rock geochemical analyses for the Grasberg deposit were provided by Freeport from proprietary databases. These data were obtained by in-house XRD analysis of pulps from 2730, 3m length half-core samples at an average 75m spacing throughout the deposit, and whole rock geochemistry data was obtained by commercial ICP analyses of splits from the same pulp samples.

2.2 Analytical methods

2.2.1 Scanning Electron Microscopy

FEI ™QEMSCAN (Quantitative Evaluation of Minerals using Energy Dispersive Spectroscopy and referred to in this paper as QEM) provided detailed mineral mapping at pixel step size resolutions of 5 μm. Resolution is here defined by the step size between point scans in the QEM-EDS mineral map. Mineral maps are constructed digitally, pixel by pixel, using look-up routines with reference X-ray mineral spectra. Spectral fit ratios less than 90% were rejected and in all such cases compositions verified using quantitative, fully calibrated FESEM EDS spot analyses and micro-XRD. The quantitative EDS spot analyses were performed at 15kV and 0.6nA of probe current using a Hitachi 4300 FESEM equipped with an Oxford INCA EDS analytical system. The system was calibrated using Astimex mineral reference standards and PAP matrix corrections (Pouchou et al., 1991) were used throughout. The colour schemes for mineralogy have not been standardized through this paper so that images presented may focus on key features of the data.

2.2.2 High resolution Scanning Electron Microscopy (SEM)

Preliminary electron backscatter diffraction (EBSD) data and high resolution SEM images were also collected on a Zeiss Gemini 450 FEG-SEM in the SEM Shared Research Facility at The University of Liverpool (Gardner, unpublished). These data provide information on the crystallographic relationships between primary and alteration feldspars that will be reported separately.

2.2.3 Powder X-ray Diffraction (XRD)

Powder XRD was carried out on a flat, solid sample blocks that were the opposing cut-off to that used for QEM mineral mapping. The analyses were performed with CoKα radiation using a Malvern Panalytical Empyrean Series 3 which is equipped with Bragg-BrentanoHD divergent beam optic, a motorized xy-stage with z-adjustment and a PIXcel3D detector (1D scanning mode, 3.347° active length), over a range of 4-90° 2Θ, with step width of 0.0131303° 2Θ and a total dwell time of 75 s/step. Phyllosilicate crystallinity standards (Warr 2018) were analysed over a range of 8-11° 2Θ, and the width of their 001-reflection compared with that of sample GP. Phase identification was carried out with DiffracPlus Eva 10 software (Bruker, 2004) and the ICDD PDF-2 database (Data, 2004).

2.2.4 X-ray Micro-computed Tomography

3D mineral distribution data were obtained by X-ray micro-computed tomography (X-ray μ-CT) using a combination of helical scanning, image registration and segmentation for quantitative analysis (Kingston et al., 2011; Sheppard et al., 2004; Varslot et al., 2011a; Varslot et al., 2011b). These data were obtained on the National Laboratory for X-ray Micro-Computed Tomography (CT Lab) at the Research School of Physics at the Australian National University using a HeliScan μCT system with an optimized space-filling trajectory to yield sharp images. The CT scanning systems are capable of imaging materials with a wide variety of densities and sizes, from 70 mm cores of rock that are imaged at 20 μm resolution, to subsection of cores <5 mm across that are imaged with a voxel size of <2 μm. The scan data were quantitatively analysed using in-house developed Mango and Drishti visualization software (Limaye,2012).

Microporosity distribution was obtained using a two-step process in which the sample was first scanned in a dry state and then in a "saturated" state after pressure impregnation with diiodomethane (CH_2I_2), which is a highly X-ray attenuating liquid. The saturation process involved immersing the sample in a CH_2I_2 bath under a pressure of 41MPa for 1-2 days. Both 'dry' and 'wet' (saturated state) scans are then brought into perfect alignment (Latham et al., 2008) and a 3D difference image created. This image shows only the attenuating liquid response (Fogden et al., 2014; Golab et al., 2010; Zhang et al., 2017) thus, creating a map of the connected porosity, including fractional porosity at the sub-voxel scale.

The dry image enables mineral groups to be classified and segmented via phase attenuation. The saturated image exhibits higher x-ray attenuation in the connected saturated pore space, enabling its connected porosity to be calculated. For a population of n voxels, the voxel porosity as volume percent is the sum of the fractional infill porosity of each voxel divided by the total voxels in the sampled region. Further segmentation of domains such as phenocrysts and veins was then conducted.

2.2.5 Thermal neutron micro-computed tomography

High throughput thermal neutron micro-computed tomographic scans (Smith et al., 2021) were conducted using the Dingo neutron imaging instrument (Garbe et al., 2015), located at the 20 MW Open-Pool Australian Lightwater (OPAL) reactor housed at the Australian Nuclear Science and Technology Organisation (ANSTO), Lucas Heights, New South Wales, Australia. These data supplement the X-ray μ-CT scans and aid the 3D mapping of veins and discrimination of mineral phases as discussed elsewhere (Voisey et al., 2020; Williams et al., 2017). For this study, Dingo was configured in high-intensity mode with a collimation ratio (*L*/*D*, where *L* is the neutron aperture-to-sample length and *D* is the neutron aperture diameter) of 500 and neutron flux of 4.75 × 107 $n.cm^{-2}.s^{-1}$ at the sample position. For all specimens, a Zeiss Ikon 50 mm f/2.0 Makro Planar lens and 200 × 200 mm × 100μm thick ZnS(Ag)/6LiF scintillator screen (RC Tritec AG) were used to obtain a pixel size of 1019 × 101 μm and Field-of-View of 200 x 200 mm. A total of 897 equiangular shadow-radiographs of 2.25s exposure was obtained as each sample was continuously rotated about its vertical axis at a rotation speed of $0.08°s^{-1}$, for a scan time of 37.5 min. One-hundred dark (closed shutter) and beam profile (open shutter) images were obtained for normalisation of the raw 16-bit radiographs. Tomographic reconstruction was accomplished using Octopus Reconstruction v.8.8. The complementary neutron and X-ray μCT data were integrated into a single registered data set for visualisation and data analysis. For the high resolution Dalam Diorite G2 and G7 sub-core QEM data were registered into the X-ray μCT data to allow 3D resolution of some mineral phases like anhydrite as described in the text.

3. Analytical Results

All of the samples analysed here are from the Dalam Fragmental Andesite (Tgdfa) and Dalam Diorite (Tgdd) geologic units, both of whose names are simplified field terms. All samples have been altered to phyllic (illite/muscovite) or potassic (K-feldspar-rich) ('potassic') assemblages during porphyry copper alteration. Based on preserved surface outcrop of volcaniclastics from the maar eruption (Mernagh et al., 2020), these samples came from 900 to 1700 m below the paleosurface that is estimated to have been at 4500 ±200 metres above presentday sea level, resulting in estimates of maximum paleo-lithostatic pressures from 22.6 to 46.9 MPa (226 - 469 bar) based on an average rock density of 2600 $kg.m^{-3}$ (Table 3).

3.1 Potassic altered Dalam diorite (G2)

Sample G2 (mine reference number GRD36-02 18.8m) is from a drillhole collared underground within the center of the Grasberg deposit. It is a weakly potassic altered Dalam diorite interpreted as an occluded block within Dalam Fragmental Andesite (Figure 4). It is paler in color than normal andesite volcanics and, through preservation of its porphyritic texture, is one of the least altered Dalam rocks found at Grasberg. Its state of partial alteration makes it particularly valuable with respect to unravelling the chemical processes involved in alteration.

QEM mineral mapping at a step size resolution of 5 μm highlights the distribution of mineralised veinlets (Figure 5) that cut the altered rock. An unmineralised quartz vein is truncated by mineralised veinlets and crisscrossed by an array of K-feldspar and anhydrite-filled fractures containing albite, bornite and chalcopyrite. This mineral mapping clearly shows the preserved, abundant primary plagioclase and biotite (*sensu lato*) phenocrysts within a

matrix dominated by K-feldspar. Also, K-feldspar with isolated albite grains infills the principal central fracture-vein that also contains anhydrite-chalcopyrite-bornite. The relative proportions of each phase are shown in Table 4 based on QEM mineral mapping.

Anhydrite is distributed through the matrix but most prominently infills discontinuous, arrays of microfractures throughout the early quartz veins and the rock matrix and is very closely associated with chalcopyrite and bornite (Figure 6). Apatite is also dispersed through the matrix and some altered biotite phenocrysts and is closely associated with anhydrite indicating its formation during alteration. The partially altered plagioclase phenocrysts (Figure 5 and Figure 6) have anastomosing veinlets of albitic plagioclase that nucleate at the vein interface and spread out from the anhydrite-K-feldspar-Cu-Fe-sulphide in the vein. The albitic composition of altered plagioclase grains adjacent to this albitic network indicate that the alteration of andesine (An_{25-50}) composition primary plagioclase resulted in loss of calcium. Quartz is heterogeneously distributed as ragged clusters but is absent in some regions, and its rounded and embayed form suggests that it has been partially dissolved. Most notably, quartz is absent from orthoclase reaction rims around plagioclase phenocrysts (X in Figure 6). Minor illite/muscovite (determined by matching corresponding Xray spectrum) is directly associated with phlogopitic biotite within interstitial voids across the partially altered plagioclase phenocrysts but absent from the K-feldspar-rich matrix and the phlogopitic biotite within it.

EDS spot mineral analyses of feldspar in the site of interest (SOI 1) demonstrate the wide range of individual feldspar compositions formed within the anastomosing veinlets and the feldspar matrix as alteration proceeds. K-feldspar and Ca-rich anorthoclase also infill grain boundary porosity resulting in a complex spread of compositions in a feldspar ternary plot (Figure 7). In a series of random spot analyses, Paterson (2004) noted the presence of some albitic plagioclase grains and suggested that these were remnants of primary oscillatory zoning in plagioclase phenocrysts. However, our data suggest that these grains form part of the anastomosing network of replacement zones that developed within primary plagioclase phenocrysts. We found no evidence of oscillatory zoning in the limited number of samples examined in this study. At higher magnification and a 1µm step size resolution, the plagioclase alteration is seen (e.g., areas Y and Z) as pervasive with two discrete anastomosing zones of albitic plagioclase veinlets cementing a mosaic of plagioclase grains of varying composition from andesine (assumed to be the primary igneous plagioclase) to albite, and b) a similar pattern of K-feldspar linked to embayment of the phenocrysts along their boundaries with surrounding orthoclase (Figure 6, area Y).

3.1.1. Biotite replacement. Concurrent with plagioclase alteration, both the matrix and primary magmatic biotite phenocrysts were intensely altered (Figure 8). Altered biotite phenocrysts retain their overall shape but have been extensively replaced, dissected and infilled by K-feldspar and are characteristically mantled by K-feldspar and quartz grains. EDS spot analyses of the large biotite phenocrysts in SOI 2 are plotted with the comprehensive biotite data set of Paterson (2004) in Figure 9. Paterson (2004) reported 'biotite' compositions from weakly to strongly altered rocks throughout the Grasberg deposit according to lithology and degree of alteration, and he also noted that even sharply-bounded magmatic phenocrysts showed evidence of weak alteration. This is demonstrated in Figure 9 with our data from the skeletal plagioclase phenocrysts in SOI 2 that corresponds to Paterson's group of partially altered magmatic biotite. Paterson (2004) also recognized green biotite that occurred on the margins of hydrothermal brown biotite and noted that hydrothermal biotite was commonly associated with magnetite. The composition of hydrothermal biotite shows a loss of Fe relative to Mg and a loss of Ti compared to less altered magmatic biotite (Figure 9), and the proportion

of K in the altered biotite is constrained between 1.55 and 1.75 atoms per 44 atoms of oxygen in the formula unit. More importantly, since the abundance of primary biotite phenocrysts is similar to that of primary plagioclase (Paterson, 2004), the dissolution of biotite during alteration caused a significant release of K into the hydrothermal fluids. Concomitant loss of Fe, as discussed below, from magmatic biotite as well as from amphibole (Paterson, 2004), may additionally have contributed Fe directly to the deposition of Cu-Fe sulphides (chalcopyrite, bornite) in pore spaces and mineralised veins.

3.2 Potassic altered Dalam Fragmental Andesite (G7)

By contrast to G2, this core sample (Figure 4) is intensely altered to orthoclase-rich potassic assemblages with only remnant altered biotite phenocrysts and is cut by arrays of quartz veins.

The high resolution (5 μm) mineral map of G7 (Figure 10) is dominated by K-feldspar (Table 4). EDS spot analyses shows that this phase is composed of about 90 to 100 mol.% orthoclase with minor calcic albite (up to 2 mol.% Ca) and equivalent 'perthitic' albite with orthoclase lamellae up to about Or_{20}. Quartz microveins are more abundant within a millimetre of the larger quartz vein (Figure 10). The quartz veins all have corroded margins and are traversed by networks of anhydrite with apatite, K-feldspar and both discrete chalcopyrite and bornite and intergrown examples. Grains of corundum with lesser andalusite and diaspore occur adjacent to highly altered ragged biotite phenocrysts. Apatite is also relatively common and is often closely associated with anhydrite and sulphides. The sample retains outlines of what we interpret to be magmatic biotite (Paterson, 2004), based on petrographic observations of less altered rocks. XRD confirmed the presence of accessory illite/muscovite, and EDS analysis showed that its K/(Na + K) was 80 - 88 wt%. This minor phase occurs as a dusting through the alteration as albitic and potassic feldspar and the altered magmatic biotite suggesting that it is a waning phase that developed during cooling of the altered rock mass in the presence of infiltrated groundwater or trapped condensate of the magmatic vapour. Discontinuous masses of anhydrite occur throughout the intensely potassium altered rock mass and notably these cut brittle fractures in earlier quartz veins (Figure 10). The latter have irregular margins indicating quartz dissolution and some of their infill consists of potassic feldspar. Clusters of intergrown chalcopyrite-bornite grains occur throughout the altered rock and are very closely associated with anhydrite in the fractured and mineralised quartz veins.

3.3 Phyllic altered Dalam Fragmental Andesite (GP)

An outer phyllic alteration zone characterizes the majority of porphyry copper deposits (Lowell and Guilbert, 1970; Meyer and Hemley, 1967) and is characterized by a range of potassic phyllosilicates from sericite (fine-grained potassic, illite/muscovite, illite). In many cases these minerals overprint earlier potassium silicate alteration (Beane, 1982; Parry et al., 2002) but, at Grasberg, they constitute a primary outer alteration zone defined by sericite and illite/muscovite phyllosilicates with quartz, pyrite and anhydrite (Paterson, 2004).

Figure 11 is a QEM mineral map for the open pit sample, GP, that was taken from the phyllic-alteration annulus around the potassic centre of the deposit. It is discussed here in the context of potassium silicate alteration at Grasberg for which comprehensive mapping of phyllosilicate distribution has been provided by Paterson (2004). In sample GP, an anhydrite-bornite infilled anhydrite-cpy-bn vein cuts through pervasively phyllic-altered and silicified Dalam Volcanic host rock. XRD analyses of the phyllic assemblage confirmed the presence of quartz, illite,

anhydrite, pyrite and traces of alum and amarantite (a ferric iron sulphate hydrate). The dioctahedral mica, was identified as well-crystallized illite similar to the epigenetic standard sample SW7-2012 (Warr, 2018).

All plagioclase and ferromagnesian silicates (biotite and hornblende) phenocrysts have been completely replaced by illite in this sample. Although some distal pore space contains very small intergranular calcite grains, the primary Ca component has been removed from the bulk of the wallrock and deposited within anhydrite. This confirms that alteration and anhydrite-sulphide deposition were contemporaneous rather than separate events. A small zone containing intergranular calcite occurs distal to the vein which, as discussed below, we interpret to be due to depletion of SO_2 from the intergranular gas flow as anhydrite formed.

The amarantite identified in the XRD analyses, and also noted in FESEM analysis, occurs with minor alums (also noted in XRD) and is likely the result of recent supergene reactions within the open pit where the sample was collected. We also noted the presence of native sulphur as a supergene reaction product at the interface of anhydrite and pyrite in the sulphide vein immediately above the top of the sample section shown in Figure 11. Paterson (2004) has noted the rare presence of kaolinite in phyllic zone assemblages and this, along with the sulphur and alum minerals, suggests that locally there was weak low temperature alteration superimposed on the potassium silicate alteration zones.
.

4. Porosity and fluid inclusions

While fractures and connected porosity are essential to the mass transport of components during the alteration of host rocks, their distribution is seldom reported in alteration studies. Norton and Knapp (1977) provided porosity and permeability data for altered igneous rocks based on laboratory and field observations of fracture arrays.

The distribution of micro-porosity in part of the polished section of Figure 6 is illustrated in Figure 12. More complete 3D mapping of the connected sub-voxel (<5.3 μm) micro-porosity through the G2 sub-core sample is shown in Figure 13a, Which also shows the tomogram of sample G2 while Figure 13b shows a slice through the tomogram corresponding to the mineral mapped section shown in Figure 5 and described above. This slice provides details of the microporosity through the altered feldspars at the margin of an altered plagioclase phenocryst and in the K-feldspar-rich matrix in the region Y outlined in Figure 6a. The micropores have diameters of up to a few microns and are located primarily on grain boundaries and triple junctions between grains. The μCT analyses allow identification of the connected microporosity that controls reactive fluid transport through wallrock during its alteration and mineralisation. Following CH_2I_2 saturation, μCT images of a longitudinal slice of the scanned sub-core of sample G2 show high porosity around the anhydrite-sulphide veins and abundant connected microporosity throughout the host rock, especially within partially altered plagioclase and biotite phenocrysts. The saturation process defines connected porosity which, for sample G2, is estimated at 2.5 volume % of the scanned sub-core. In the colored microporosity slice of the X-ray CT tomogram (Figure 13b) small isolated clusters of voxel porosity >10 volume % are shown in red and < 1% are shown in blue, where voxel porosity is the volume of pore space in each voxel that contains CH_2I_2. These microporosity data show high porosity along the anhydrite-sulphide infilled veins that may be due to thermal contraction, shear movement on the vein or localized later dissolution of anhydrite.

In a sub-sample of G7, the porosity distribution (Figure14) contrasts strongly with the microporosity of the partially altered sample G2. In G7 the quartz-filled veins have almost no remaining porosity indicating the efficient sealing of the fractured vein by anhydrite, sulphides and some intergranular feldspar. Of particular note is the much lower relative porosity of the orthoclase feldspar matrix than the clusters of feldspar-and phlogopitic biotite that replace primary biotite phenocrysts. This may indicate that feldspar recrystallization has removed intergranular pore space.

In a rock mass undergoing alteration due to fluid saturation there is a continual process of generation and sealing of connected porosity. Sealed micropores at all scales may become fluid inclusions that potentially allow trapped fluid (liquid or gas) to be preserved so that, with necessary care to avoid leaked inclusions or interchanged components (Lerchbaumer and Audétat, 2012), it is possible to estimate the ambient fluid composition at the site of trapping. Fluid inclusion homogenization temperatures for liquid phase (condensate) inclusions in quartz veins record temperatures that are below the temperature of the ambient isentropic expanding magmatic gas phase. This mismatch of inclusion homogenization temperatures and mineral relations is common in porphyry copper studies, particularly where liquid phase continua models are assumed. Detailed discussion of the fluid inclusion populations at Grasberg have been provided elsewhere (Mernagh et al., 2020; Mernagh and Mavrogenes, 2019) so that only a brief summary is given here. No intermediate density fluid inclusions were found in the study of Mernagh and Mavrogenes (2019). Only, two types of aqueous inclusions were observed in quartz veins. The first type were high salinity inclusions containing a large halite crystal ± sylvite, a small opaque crystal and a vapour bubble. Their salinity ranged from 39.3 wt% NaCl eq. to 54.0 wt% NaCl eq. Total homogenisation or partial homogenisation (V+L+S→L+S) temperatures ranged from 356 °C to 602 °C. The second type were lower salinity, aqueous inclusions containing 15 – 30 vol.% vapour that were clearly of secondary origin and these homogenised to liquid over the range 234 – 458 °C. A third type of inclusion occurred in early vein quartz. These inclusions contained primary and pseudo-secondary trails with abundant multi-solid inclusions (MSI) containing halite, sylvite, anhydrite, hematite, chalcopyrite, pyrite and other unidentified crystals. Vapour bubbles typically filled ~20 to 30 vol% of inclusions. These MSI have salinities ranging from 65 to 75 wt% NaCl eq. and do not completely homogenise, but instead form a liquid brine and coexisting liquid silicate that remain immiscible at temperatures up to 1281 °C (Mernagh and Mavrogenes, 2019). These ultra-high temperatures and salinities may be ascribed to the entrapment of hydrated molecular clusters (i.e. salt hydrates formed in the vapour phase) during crystal growth (Henley and Seward, 2018). Alternatively, if interpreted as inclusions that grew within quartz veins during episodes of isenthalpic expansion into fractures, then the primary inclusion temperatures represent transient growth conditions rather than the temperature of the ambient continuum fluid within the magmatic vapour plume at that depth. These temperatures are thus compatible with those estimated through analysis of phase assemblages. For the current study suitable inclusions were sought unsuccessfully in alteration feldspar and anhydrite, however, in the latter, inclusions were vapour-rich (Figure 15). These inclusions are rare and appear to be primary, i.e., associated with the growth of anhydrite. Unfortunately, due to their small size and the fact that inclusions trapped in anhydrite are prone to leakage, they were not further analysed. Moreover, the mineral sequences described in this paper emphasize that sulphate-sulphide mineralisation occurred from a *quartz-undersaturated gas phase* that post-dated earlier episodes of quartz vein formation.

5. Discussion

Potassium silicate alteration at the cubic kilometer scale characterizes porphyry copper deposits worldwide. This paper provides new data targeted at developing more rigorous understanding of how such alteration develops by replacement of primary host rocks and how alteration processes may be directly related to the deposition of base metal sulphides in porphyry copper deposits. This analysis is based on a multidisciplinary approach that combines aspects of fluid flow, brittle rock failure, phase relationships and basic gas properties with the mineralogic observations detailed above. In order to commence this analysis, it is however necessary to restate some important fundamentals.

5.1 Fundamentals of fluid phase mass transfer in the porphyry copper environment

The first fundamental concerns the matter of scale. Mineralisation and alteration in porphyry copper-gold deposits developed within *magmatic vapour plumes* (Henley and Berger, 2013; Henley and Hughes, 2016; Henley and McNabb, 1978; Weis et al., 2012) that were fed by magmatic vapour expansion from deeper, crystallizing intrusion complexes. Figure 16 illustrates the basic anatomy and extent of such a volcano-scale magmatic vapour plume in relation to the Grasberg diatreme and the porphyry copper-gold deposit. The scale of the latter (a few cubic kilometres) is only a fraction of the scale of the plume and confined to the specific outflow regime that is centred on the highly permeable breccia within the diatreme vent. Porphyry copper deposit formation occurs over a period of at most a few tens of thousands of years and, as in the Grasberg district (Leys et al., 2020), several plume events may occur through the lifetime of the magmatic province.

An implication of the schema for the Grasberg plume, as shown in Figure 16, is that the magmatic fluid was derived from a deep complex of intrusions which themselves may have interacted directly with deeper sources of gas components including metals and sulphur. It is also implied that the deposit scale phyllic and potassic alteration is a consequence of gas-solid reactions driven by such 'magmatic' gas rather than involving external groundwater as is demonstrated both at Grasberg (Harrison, 1999) and El Salvador (Watanabe and Hedenquist, 2001) using stable isotope transects. The viability of magmatic gases for metal transport in developing porphyry copper systems has also been investigated by multicomponent equilibrium thermochemical modelling and theoretical simulation of alteration and mineralisation (Henley and Seward, 2018; Hurtig et al., 2021).

The second fundamental requiring emphasis is that, regardless of its phase state, mass transport is governed by the physics of fluid flow through fractured porous media (Berre et al., 2019). This means that mass flux occurs through both fractures and wallrock but the flow regimes in each are, while interconnected, quite different. Flow in fractures is governed by pressure differentials through Darcy's Law but in wallrock, mass flux is governed by connected porosity (intergranular porosity, microfractures and microporosity) driven, at smaller scale, by Darcy permeability through Knudsen flow constraints. Moreover, these interactive phenomena develop as dynamical (by definition, constantly evolving) systems due to local and larger scale deviatoric stresses, including regional stress (Sapiie and Cloos, 2004). In these systems, as is demonstrated by the data reported here for altered rocks at Grasberg, mineral deposition occurs in fractures when fluid flow is throttled. A coupled fluid flow in the wallrock results in progressive alteration of primary minerals and deposition of disseminated sulphides and

anhydrite with reacted fluid feeding back into the fracture flow regimes. This contrasts with approaches that assume a uniform permeability through a rock mass or pipe-models that assume flow from some source reservoir through a simple array of fractures.

Thirdly, where reliable estimates are available for fluid phase pressure (as at Grasberg through preservation of the paleosurface) and temperature (through mineral stability relationships and systematic interpretation of fluid inclusions), then the phase state of the continuum fluid may be determined. At Grasberg and elsewhere (Mernagh et al., 2020) the phase state is that of a compressed gas. The relationships between volume, pressure and temperature in a compressed gas within a developing deposit are then controlled by the well known Gas Laws in concert with understanding of adiabatic expansion of gases (Anderson and Crerar, 1993) and heat transfer (Henley and Hughes (2016). Where a liquid phase continuum fluid is assumed for modelling purposes then pressure-temperature relationships are commonly imposed (c.f. fluids are stated to have heated or cooled) without consideration of the requirements of the laws of conservation of heat and mass. These are important as shown by Mernagh et al.(2020) who demonstrated that the maximum volume percent of saline liquid was only 2% in a magmatic two phase plume so that the continuum fluid was predominantly a gas phase. The saline liquid component may be regarded as an aerosol whose wetting properties may be responsible for the abundant liquid-dominated inclusions that are trapped during crystal growth during vein infilling even though vapour-rich inclusions are also abundant.

Finally it is necessary to revisit some of the fundamentals of fluid inclusion interpretation following Mernagh et al. (2020).The mineralised zone in porphyry copper deposits typically forms well above the magmatic intrusions that release the fluids into the porphyry systems. The fluids released from these magmas are commonly trapped in unidirectional solidification textured (UST) quartz which is spatially associated close to the intrusions. This UST quartz has only rarely been observed in porphyry deposits (e.g. Carten et al., 1988; Bain et al., 2022). However, most fluid inclusion studies are conducted on inclusions occurring in quartz veins formed at higher levels within the brittle environment of the porphyry deposits. As a consequence, the fluid inclusions present in the quartz veins trap vapour or liquid that have substantially evolved after their release from a source magma. Processes such as phase separation increase the concentration of many elements within separated liquid relative to the vapour phase, and, as stressed in this paper, fluid phases are partially or completely equilibrated with the host rock through which they pass. This process of fluid-rock equilibration is evident in Figure 5 of Kouzmanov and Pokrovski (2012). In this figure the elemental concentrations in single-phase, vapour-rich, hypersaline and low-salinity aqueous fluid inclusions vary as a function of their salinity. However, the ratios of each element to each other (i.e., the elemental patterns) of the average values are very similar for all four types of inclusions. This would not be expected to occur in inclusions that were trapped during separate fluid flow events unless they had equilibrated with the host rocks.

Recent models for the fluid evolution of porphyry copper deposits suggest that an initial, single-phase, “supercritical” fluid is exsolved from the magma (Kouzmanov and Pokrovski, 2012). Fluid inclusions thought to represent this supercritical fluid are referred to as ‘intermediate density’ inclusions but this definition is not well constrained. Kouzmanov and Pokrovski (2012) state that these inclusions contain approximately equal volumes of liquid and vapour at room temperature while Audetat (2019) states that their salinity lies between 5 and 15 wt % NaCl eq. and Hurtig et al. (2021) defines intermediate inclusions as having

densities from 0.1–322 kg/m^3, which is an enormous range. However, all authors agree that these "supercritical" fluids behave like gases in magmatic vaour plume environments. Therefore, we suggest that the term "intermediate density" inclusions is causing a great deal of confusion in the literature and this should be avoided by referring to the state of the fluid at the time of trapping (either gas or liquid) and avoiding terms like liquid-like that simply obfuscate understanding of reactive mass transfer in these environments. By doing this, it would become immediately clear that gaseous fluid (often referred to as 'vapour') are predominant in all stages of fluid evolution in porphyry copper systems. The term 'vapour' itself has a specific meaning which is that it is a gas *in equilibrium* with a condensed phase (solid or liquid). A further consideration is that condensed liquid is necessarily saturated with gas phase species and that these solutes contribute to the apparent salinity that is deduced from freezing point measurements as discussed by Hedenquist and Henley (1985).

With these fundamentals in place, the processes that developed zoned potassium silicate alteration at Grasberg may be examined through analysis of the available deposit scale geochemical data and the mineralogical data described above. Here we take an inductive analytical rather than attempt a numerical modelling approach given the complexities of the interacting flow regimes.

5.2. Element transfer

The high-resolution petrographic data that has been presented above show that the development of vein-filling and intergranular anhydrite and sulphides is coincident with the alteration of primary plagioclase phenocrysts and their matrix. It is evident that Ca is progressively transferred from the plagioclase into anhydrite so that the assemblage is sub-divided into silicate and sulphide-sulphate sub-assemblages. A consequence of the sequestration of Ca to anhydrite is the redistribution of alkalis into potassic alkali and sodic plagioclase feldspar (Figures 5 and 6) through the altered phenocrysts as well as into the developing veins. Primary magmatic biotite is also altered with the release of iron. This alteration process only requires the addition of sulphur and copper, with HCl primarily operating as a flux or complexing agent; for the transport of alkalis and copper as gaseous chloride species. HBr also acts in this way (Henley and Seward, 2018). Summarized in this way it is possible to suggest that alteration at the local scale is essentially isochemical, given that some alkali is lost into the larger scale vein flow. This loss is small given the very low solubility of silicate minerals, as are the solubilities of anhydrite and sulphides. We therefore suggest that with the exception of a flux of S as SO_2 (Henley et al., 2015), HCl and Cu ($\pm$ Au, Mo), alteration and mineralisation are coupled and essentially isochemical. It suggests that potassium silicate alteration is a consequence of Ca sequestration resulting in a K-enriched silicate sub-assemblage whose potassium concentration has been further enhanced by sequestration of Si into earlier quartz veins. The corollary is then that potassium silicate alteration does not require the addition of potassium through influx of an exotic brine or potassium enriched magmatic fluid as has previously been assumed. Our data also show that alteration and mineralisation occurred with silica undersaturated in the reactive gas mix leading to progressive dissolution of earlier vein quartz and primary host rock quartz. We shall refer to this proposal as the *quasi-isochemical hypothesis for potassium silicate alteration*.

The quasi-isochemical hypothesis for potassium silicate alteration proposed above may be tested at the larger deposit scale. Figure 17 provides comparison of the compositions of weakly

altered Dalam intrusive and volcanic rocks (Table 5) with the averages of altered and mineralised rock compositions within the deposit. Since all the primary (unmineralised) Dalam rocks have suffered weak deuteric alteration as is common in volcanic sequences, their compositions have been normalized to a water and sulphur free basis but their average LOI values are shown as the bar D in Figure 17. Notably, D is close to the average LOI for phyllic altered rocks but higher for potassic altered rocks whose range of LOI and SiO_2 values is large. The wide compositional ranges for altered rocks are hard to interpret especially where potassic altered rocks appear to show lower K_2O than unaltered Dalam host rocks. However, since the altered and mineralised rocks differ from unaltered rocks through hydrolysis (for phyllic alteration) and the addition of sulphur and metals including Cu, the comparison is more usefully made on the basis of normalization to molal abundances with exclusion of these added components. This approach, depicted in Figure 17 shows that there is a remarkable similarity between unaltered Dalam igneous rock compositions and those of the average potassium silicate altered rocks. Outliers in these data are few and this suggests that element redistribution occurs mostly within the 3m scale of the samples up to deposit scale.

The correspondence between the major element compositions of primary (i.e. least altered surrounding rocks) and potassium silicate altered igneous rocks at Grasberg affirms that the *major elements* of the primary igneous rock mass are conserved during deposit formation and that porphyry copper deposit formation is the simple result of adding water, metals such as Cu and Mo, and SO_2, the latter disproportionating to form sulphide and sulphate minerals through reaction with plagioclase to form anhydrite (Henley and Fischer, 2021; Henley et al., 2015). In this process HCl plays an essential catalytic role through formation of gas phase vapour transport species for the major elements as well as for metals including Fe and Cu. The system itself is open to input of magmatic vapour and discharge through to the surface so that while major elements are redistributed at a variety of scales in the developing deposit through their low solubilities, they are essentially conserved at the deposit scale. These observations then suggest that porphyry copper alteration and mineralisation are essentially isochemical (quasi-isochemical) except for addition of sulphur and the ore metals (Cu, Mo, Au, etc). Losses of alkali metals are limited by the very low solubilities of silicate, sulphate and sulphide minerals.

A corollary of the quasi-isochemical hypothesis is that potassium silicate alteration assemblages are the consequence of Ca sequestration into anhydrite as is illustrated by the ternary plot for Al_2O_3-CaO-K_2O-MgO in Figure 18. This process necessarily shifts the composition of the remaining silicate sub-assemblage along a tie line to the muscovite or K-feldspar stability fields depending on the pressure and temperature of alteration. Ca sequestration to anhydrite therefore necessarily induces potassium silicate alteration without any other mass transfer beyond addition of sulphur as sulphate, and, for phyllic alteration, water. This sequestration process is complimented by the alteration of primary magmatic biotite to phlogopitic biotite plus K-feldspar. Another corollary is that deposition of iron-bearing sulphides (pyrite, chalcopyrite, bornite) is in response to the in situ H_2S formation as anhydrite is formed, with Cu supplied in the magmatic gas flux. The Fe required for copper sulphide and pyrite deposition is also provided by the magmatic gas input as well as locally by the dissolution of biotite as well as amphibole and the minor Fe released from primary plagioclase.

It is important to note that the quasi-isochemical hypothesis proposed here is not amenable to mass balance examination through Gresens isocon modelling (Grant, 1986) because the alteration assemblages, at sample scale, are an intimate mixture of silicates and anhydrite as well as sulphide minerals. At a basic level the defined resources of Cu (5.26 Gt) and other

metals in the deposit are an expression through grade (~ 0.61 % Cu) of the mass of copper and sulphur added to the primary rock by the reactive flux of magmatic gas. Moreover, the process of potassium silicate alteration itself results in quite large variations in local compositions. For example, at the sample scale (split drill core in lengths of 3m), the composition of some samples may be affected by large numbers of earlier quartz or other veins as exemplified in the sample photographs shown in Figure 4.

We may however recalculate the respective volumes of phyllic and potassic alteration at Grasberg (Table 2) as masses using appropriate rock density data from the deposit, in order to obtain the minimum, overall water:rock mass ratio responsible for the formation of the deposit. Here the density of the altered rock mass is taken as that of feldspar (2560 kg/m^3) and the average whole rock LOI due to biotite and muscovite/illite is taken as 2 wt% in order to include water within these minerals. The S content of the altered rock mass is converted into moles of total sulphur and in turn to an equivalent mass of water (1.27E+13 kg) based on the representative volcanic gas analysis provided in Table 6. The time integrated minimum water:rock mass ratio is higher in the phyllic than the potassic alteration assemblage and their overall ratio is 2.24 (Table 7).

The recognition that, owing to the exceedingly low solubilities of sulphide minerals, anhydrite formation with release of reduced sulphur is directly coupled with sulphide deposition allows us to estimate the minimum concentration of copper in the magmatic gas phase that fluxes through to the developing deposit. Thus the total estimated in-situ Cu metal content of 32 Mt Cu was introduced by the minimum mass of water (1.27E+13 kg), so that the minimum concentration of Cu in the magmatic gas phase was ~2500 mg/kg. This compares very favorably with the value of 3000 mg/kg Cu in the single-phase magmatic input gas at Grasberg that was used by Mernagh et al. (2020) to track the systematics of Cu partitioning between vapour and liquid during two phase expansion during deposit formation. This adopted value itself was based on fluid inclusion data for Grasberg reported by Ullrich et al. (1999).

Although the focus of this paper is on potassium silicate alteration processes during porphyry copper formation, it is interesting as an aside to compare these estimated gas phase compositions with those observed in fumaroles on active volcanoes. Zelenski et al. (2013), for example, reported 2 ppm Cu in the 1084 °C gas mixture discharged from hornitos immediately adjacent to basalt magma at Erta Ale (Ethiopia). Such proximal magmatic gas data are not available from the less quiescent magmatic arc andesite volcanoes but Wahrenberger (1997) reported 53 ppb for a 920 °C fumarole on Kudryavy Volcano (Kurile Islands, Russia). Notwithstanding the difference in provenance of their source magmas, the large difference (~40 times) between these measurements together with the absence of Cu minerals in arc volcano fumarole sublimates led Henley and Berger (2013) to propose that subsurface deposition of Cu from volcanic gases was highly efficient. The subsequent recognition of the coupling of anhydrite formation with in situ H_2S formation (Henley et al., 2015) supports this hypothesis as does the petrographic data reported in this paper. A further implication is that the formation of major porphyry copper deposits requires source magmas that are highly enriched in copper and other metals relative to other arc magmas as discussed by Park et al. (2021) and Chiaradia and Caricchi (2022).

In terms of volcanic context, it is useful to speculate on what may have been the paleo-surface environment above the developing Grasberg porphyry copper deposit. A maar lake has been recognized through preservation of some of its marginal volcaniclastic sediments (Mernagh et al., 2020) in the rugged, high altitude, mountainous terrane within which the deposit occurs.

Mineralisation and alteration were occurring to only a few hundred metres below the surface (Figure 3) so that it is likely that there were widespread gas discharges through the lake floor to produce a hyperacidic lake, as well as subaerial fumaroles and these continued during the late stage Kali resurgence. Excess SO_2 and H_2S that discharged likely produced sulphur-bearing sediments and floating sulphur globules some of which may contain crystals of covellite (CuS) and enargite (Cu_3AsS_4) as is observed at Kawah Ijen in east Java (Henley, 2015). A similar surface environment appears to have been developed in proximity to the evolving Far Southeast porphyry copper deposit in the Philippines (Berger et al., 2014) as well as at Jardin in Chile (Lortie and Clark, 1987). In other porphyry copper environments the consequence of discharge and condensation of excess acidic gas through near surface fractured rock is expressed through the development of 'high sulphidation' copper, arsenic, gold mineralisation in solfatara (Berger and Henley, 2011, Henley and Berger, 2011) as is exemplified at Chinkuashih, Taiwan (Henley and Berger, 2012), Pascua Au–Ag–Cu deposit, Chile and Argentina (Chouinard et al., 2005, Deyell et al., 2004) and other deposits even though economic grade porphyry copper mineralisation may not occur below them.

Returning to the focus of this paper (the hypothesis that potassium silicate alteration during porphyry copper formation does not require significant gain or loss of major elements) we proceed below to consideration of the pressures and temperatures of the alteration environment and then to a more detailed examination of As noted above, alteration processes.

5.2 Pressure

Alteration and mineralisation in porphyry copper deposits are the result of the flux of magmatic gas from source to surface. The principal components of the gas phase (Table 6), as discussed elsewhere, are of similar composition to that sampled in active volcanoes (Henley and Berger, 2013; Henley and Seward, 2018). Volcanic gas compositions are dominated by H_2O, SO_2 and HCl, with some HF also present. Metals such as Cu, Mo and Au are transported into the porphyry system in such magmatic gas and precipitated as a consequence of the in-situ generation of H_2S by anhydrite-forming reactions (Henley et al., 2015; Henley and Seward, 2018). As noted above, the continuum fluid within a magmatic vapour plume (Henley and McNabb, 1978; Weis et al., 2012) is a condensable gas phase containing up to only a few percent of salts so that during expansion within a plume, a maximum of about 2 volume percent of saline liquid condenses out (Mernagh et al., 2020). Additional evidence for the predominance of a vapour phase continuum fluid at Grasberg have also been provided by sulphur isotope analyses that show that SO_2 and H_2S were indeed the dominant species at temperatures above 550 °C and that the hydrothermal fluid followed a rock-buffered trajectory and became more reduced at < 550 °C as H_2S was progressively released during expansion (Sulaksono et al., 2021).

The altered and mineralised rocks at Grasberg and other porphyry copper deposits (Redmond and Einaudi, 2010) are characterized by multiple extensional fracture arrays. Successive generations of these fractures are the principal guides for magmatic gas throughout any evolving porphyry copper deposit. Given the maintenance of such fracture arrays in response to changing deviatoric stress, we may assume that a magmatic gas phase expands through to the surface to be discharged at close to atmospheric pressure. For a compressed gas phase expanding through low thermal conductivity porous rocks, it is reasonable to assume that expansion is adiabatic as discussed elsewhere (Henley and Fischer, 2021; Henley and Hughes, 2016). Where expansion may be considered reversible (in low permeability fractured porous rocks), the PT path is isentropic (Anderson and Crerar, 1993) and may be modelled on the basis of the properties of pure water (Wagner et al., 2008) assuming also that the few percent of other

gases in the magmatic gas mixture behave as ideal gases. Figure 19 provides a plot of isentropes (constant entropy) and isenthalps (constant enthalpy) for pure water in PT space. As will be discussed below, it is then possible to examine simple gas expansion trajectories from source to surface. Such trajectories are distinct in that temperature gradients are high with respect to pressure. By contrast, for irreversible expansion into, for example, an open fracture PT paths are isenthalpic and the temperature gradient is much lower. It is also evident from the relationship between vein and wallrock assemblages in samples G2 and G7 that a fluid phase from open fractures passes into intergranular space in the wallrock which progressively becomes choked by a sulphide-sulphate sub-assemblage and K-feldspar deposition while new connected porosity develops through mineral dissolution. The reacted gas permeates back into the fracture-guided gas flux.

In a magmatic vapour plume the internal fluid pressure must be maintained at greater than the external groundwater pressure so that groundwater does not penetrate the deposit during its formation. Such permeation does occur during the later (retrograde) waning stages of porphyry deposit formation as the pressure declines in the magmatic vapour reservoir of the system. The pressure within the plume itself is controlled by adiabatic gas expansion (as discussed above) and the effective permeability of the rock mass as it undergoes repetitive fracturing and alteration. Plume pressures may therefore be interpreted through the principles of hydraulic fracturing in response to fluid pressure cycling within stressed crust (Cox, 2010). At Grasberg the preservation of part of the paleosurface during deposit formation enables the *maximum* lithostatic alteration pressure P_{max} for each sample to be estimated through the following equation,

$$P_{max} = P_L + \Theta = \rho_r g h + \Theta \quad (1)$$

where P_L is the lithostatic pressure defined by the density, ρ_r, of the rock mass, g is the acceleration due to gravity and h is the estimated depth of the sample beneath the paleosurface. Θ is the tensile strength of the rock mass and has values up to about 5 MPa. Taking Θ as about 1 MPa (Cox, 2010), Dalam volcanic rock density as 2600 kg m^{-3} and ignoring atmospheric pressure (0.1 MPa), the upper limits of lithostatic pressures for the samples examined here are shown in Table 3. No depth estimate can be made for sample GP as the only information available is the depth of the bottom of the open pit at time of sampling. Its pressure-depth estimate is then less than that for this depth. At Grasberg, economic mineralisation extends from near the paleosurface (4500 masl) to about 2000 masl, giving a range of lithostatic pressure from 46.9 to 22.6 MPa, respectively, and hydrodynamic pressure from 16.7 to 7.8 MPa within which these processes occurred. However, whilst useful as ambient reference pressures, alteration reactions may have been initiated at locally much lower transient pressures immediately after fracture formation and throughout subsequent pressure recovery (Mernagh et al., 2020).

For a gas phase expanding to the surface, its pressure is less than lithostatic but greater than hydrostatic pressure due to liquid water at the same depth because otherwise groundwater would flood the system. This relationship allows approximation of the minimum pressure of the expanding gas phase at each sample depth (Table 3).

5.3 Temperature

Fluid inclusion data provide a general view of part of the temperature range over which porphyry copper deposits formed from expanding magmatic vapour (Mernagh et al., 2020).

Temperature estimates for alteration processes are independently obtained from key phase equilibria. Thus, samples G2 and G7, as detailed above, provide evidence that they formed in a phase regime where K-feldspar was stable and actively forming, while the phyllic-altered sample, GP, formed in a distinct regime where 'illite' was the stable potassium phyllosilicate phase that replaced primary plagioclase feldspar. Corundum and diaspore (assumed a retrograde alteration of andalusite) are present in G7. Corundum has been previously reported in association with andalusite from Grasberg (Penniston-Dorland, 1997) as well as from a number of other porphyry copper deposits including Los Pelambres and El Salvador, Chile (Atkinson et al., 1998, Gustafson and Quiroga, 1995). The presence of these trace aluminosilicate minerals allows temperature estimations for this sample through plotting the range of its estimated limits for alteration pressure onto the phase diagram for the decomposition of an assemblage of quartz and muscovite to K-feldspar, corundum and water vapour (Kerrick, 1972) as shown in Figure 19; it is important to note that the reference phase boundaries are based on experiments on pure potassium aluminosilicate mixtures and that, as shown below, some variation occurs in natural systems through the presence of other salts and due to the saturation state of silica in the gas phase with respect to quartz. The K-feldspar-andalusite phase boundary is very close to that of corundum and so choice of andalusite as reference makes no significant difference to the temperature estimate referred here. What is important is that the occurrence of corundum indicates a relatively low fugacity of silica in the gas phase and this reinforces the observation from the partial dissolution textures on quartz in the samples analyzed here indicate that potassic alteration occurred under quartz-undersaturated conditions.

In order to determine alteration processes at the scale of the deposit we need to estimate a likely expansion path in pressure-temperature space for an expanding magmatic gas. As noted above pressure on this path must be lower than lithostatic pressure in order to sustain flux of the reactive gas phase, and higher than hydrostatic. *For the purposes of discussion*, we here propose that the magmatic gas phase had entropy equal to about 6.5 $kj.kg^{-1}.°C^{-1}$ (Figure 19). This is commensurate with release of magmatic gas from intrusions at a lithostatic pressure of 50-60 Mpa and equivalent depth of > 2km. Consideration of a deeper magmatic source and consequent higher pressures along the expansion path necessarily change the assumed entropy of the released magmatic gas and temperature estimates that we have applied in the discussion by $\pm$ ~20°C but do not alter the principle outcomes of the analysis.

For this illustrative model, sample G7, therefore, alteration occurred between about 565 and 585 °C at hydrostatic pressure. Sample G2, which preserves a partially altered state, with K-feldspar replacement of plagioclase and precipitation in fractures, has an estimated alteration temperature 535-550 °C at hydrostatic pressure (Figure 19). The expansion path tracks through the upper stability limit of K-mica (muscovite) to the lower pressures and temperatures that applied for crystalline illite formation in sample GP (whose paleodepth is not well established as a loose sample of phyllic alteration) at <415 °C. Muscovite is used as a reference proxy for the range of potassium micas that characterize the phyllic alteration zone noting that the upper stability limit for pure illite is not well established. It has been recorded with crystalline muscovite at 350-360°C for geothermal wells in the Philippines (Reyes, 1990) but may be stable to higher temperatures. Its stability as a silica-rich potassium mica is also dependent on the chemistry of the coexisting fluid phase.

Along this path the density of the gas phase at G7 was about 47 $kg.m^{-3}$, 42 $kg.m^{-3}$ for G2 and < 24 $kg.m^{-3}$ for GP. For reference, liquid water at room temperature and pressure has a density of 997 $kg.m^{-3}$. This approach also suggests that the continuum gas phase was released from a

dioritic melt at about 750 °C and ~55 MPa, and had a density of about 130 kg/m^3 It expanded isentropically (~ 6.0 $\pm$ 0.2 kJ/(kg.°C) by a factor of three at the boundary between potassic and phyllic alteration zones. In a developing porphyry copper system, cyclic fluctuations of local gas pressure occurred due to hydraulic fracturing (Figure 20a). This fracturing resulted in highly variable gas phase densities as fractures opened and closed in the evolving fracture arrays (Mernagh et al., 2020). In turn these triggered rapid vein mineral deposition due to pressure effects on solubility (Crerar et al., 1985). Rapid pressure drops due to fracturing provided irreversible isenthalpic offshoot paths to lower pressure with coupled reduction of pore pressure in the host rock (Mernagh et al., 2020) and associated temperature changes. For example, if fracture formation provided a transient localized isenthalpic expansion for G2 to 10MPa then the alteration temperature would drop from 600 to 550 °C and vein mineral deposition would initiate (Figure 19).

5.4 Alteration processes

The overall context for porphyry copper formation is that of a dynamical, internally and externally stressed, gas phase reactor (Henley and Berger, 2013). Cycles of repetitive fracturing continually maintain the high permeability flow paths that are required for expansion of the continuum magmatic gas phase, from source to surface, through porous rock during its evolution as an altered and mineralised rock mass. A minor volume fraction (< 2% volume) of saline liquid condenses during gas phase expansion as is detailed elsewhere (Henley and McNabb, 1978; Mernagh et al., 2020; Weis et al., 2012). The PT data and illustrative expansion path for the magmatic gas phase that is detailed above, show that rock alteration and mineralisation at Grasberg occurred at pressures of a few tens of MPa. The temperature was > ~550 °C for potassic alteration and down to ~ 350 °C for phyllic alteration due to progressive reaction between the porous rock mass and a flux of reactive magmatic gas containing SO_2 and HCl, as well as metals including Cu, Mo and Au as gas phase species (Henley and Seward, 2018).

The generation of H_2S, as a by-product of the formation of anhydrite results in co-deposition of chalcopyrite or bornite – and pyrite in the phyllic alteration zone - through reaction with Fe released during the replacement of primary biotite by higher Mg number (Mg#) phlogopitic biotite. At Grasberg this replacement process forms a characteristically shredded texture as described above and by Paterson (2004), and this has also been documented in other porphyry copper deposits such as Alumbrera, Argentina (Harris et al., 2004) and Santa Rita, New Mexico (Jacobs and Parry, 1979). The compositional ranges of altered relative to primary magmatic biotite have been described elsewhere and confirm losses of K and Fe relative to Mg and Si-Al. The overall replacement process commonly retains the primary fabric of the original biotite (or amphibole) phenocrysts until it is well advanced, as in GP where almost complete replacement by clusters of illite and K-feldspar occurs. Replacement of amphibole also provides Fe for subsequent sulphide deposition as noted by Paterson (2004) and some Fe may also be contributed by dissolution of primary magnetite. The scattered occurrences of accessory disseminated sericite/illite and chlorite are interpreted as the product of retrograde alteration.

The overall process of potassium silicate alteration is one of gas phase dissolution and precipitation of silicate minerals at the deposit scale but with more localised types of chemical reactions developed over a range of smaller scales. Mechanisms of feldspar replacement have been discussed by several authors in the context of metamorphic terranes (Hövelmann et al., 2010; Niedermeier et al., 2009; Putnis, 2009). but we are not aware of any detailed studies of such replacement processes in hydrothermally altered rocks, or specifically for porphyry

copper deposits due to gas-solid reactions. The theory of dissolution-precipitation as the mechanism of mineral replacement has progressively evolved over the last two decades into a more explicit form focused on interface-coupled reactions (Cardew and Davey, 1985; Gardner et al., 2021; Hövelmann et al., 2010; Putnis, 2009; Putnis, 2021; Putnis and Putnis, 2007). Key features of the theory are epitaxial growth of the replacement phase onto the replaced phase, the catalytic effect of water (i.e. water is conserved), the development of microporosity in response to density differences and the presence of a liquid-like boundary layer at the reaction interface. However, in the high temperature, low pressure gas-solid reaction context, no adsorbed hydrous layer is present as a dissolution medium. Rather the mechanism centres on chemisorption that is defined as adsorption which results from chemical bond formation (strong interaction) between the adsorbent and the adsorbate in a monolayer on the surface (IUPAC, 2014); the reference to a monolayer is nominal given the formation of longer-range molecular interactions in the gas phase (Kubicki and Watts, 2018). Rather than dissolution-precipitation in this setting, it is therefore more appropriate to focus on mechanisms of element gain and loss involving lattice degradation (Henley et al., 2017; Petrishcheva et al., 2020) and nucleation of product phases such as, in the present case, anhydrite. Other differences are that ionic species are not present in a low density, high temperature gas phase and gas flux is not constrained by fluid boundary layers.

As shown in Figures 13 and 14, microporosity is abundant in samples G2 and G7 and particularly in the partially altered plagioclase phenocrysts in G2. However, in sample G2 *two* replacement processes operated simultaneously. These were the replacement of plagioclase by albite that is nucleated at the fracture vein interface in response to sequestration of calcium into anhydrite, and the replacement of plagioclase by K-feldspar that nucleates at the phenocryst interface with its more potassic, K-feldspar-magmatic biotite matrix. Sample G7 shows the completed stage of these replacement processes where all Ca has been removed from the silicate part of the mineral assemblage.

Figure 20b provides a schematic summary of the alteration process at the scale of a few cm and highlights the interaction of porous medium and fracture flow, and the input and output of major components that results in the partially potassic altered sample, G2. Continued magmatic gas flux progressively leads to the intense alteration of sample G7. In the expanding gas flux at lower temperature and pressure, equivalent flow schema applies that result in the intense phyllic alteration and mineralisation of sample GP. This same generalized schema applies at the deposit scale to provide the zoned potassium silicate alteration and mineralisation shown in Figures 2 and 3 for the Grasberg porphyry copper deposit and which is mirrored in other porphyry copper deposits worldwide.

G2, itself, preserves an intermediate, and therefore non-equilibrium, stage in the potassium silicate alteration process, and this is highlighted by the display of interlacing Na-feldspar and K-feldspar anastomosing veinlets running through the altering plagioclase from a nucleation zone adjacent to the anhydrite-Cu-Fe sulphide fracture vein. The veinlets are smaller scale and quite distinct from vein formation due to fracture infilling. The Na-rich veinlets nucleate at the boundary between the plagioclase phenocryst and the open fracture and evidently coalesce progressively as plagioclase replacement proceeds. K-rich alkali feldspar replacement of plagioclase develops also as anastomosing veinlet networks through primary plagioclase but these spread contrary to the direction of the Na-rich veinlets. These are nucleated in the replaced rims of the phenocrysts that are evident in Figures 5 and 6. Rim development in such ‘shrinking core expanding rim’ settings are a Knudsen diffusive process related to the surface area of solids in the presence of reactive fluid (Amiri et al., 2013). Reaction progress may

become self-limiting as product minerals accumulate in the interface region. In sample G2, K displaces Na from the reacting plagioclase with Na and excess K lost in the general discharge of reacted gas. This feature of the contrary growth directions of the veinlet networks and lack of ordered fabrics suggest that an origin from microfracture networks, such as associated with hydraulic fracture initiation (Ravi-Chandar and Knauss, 1984) is untenable. A diffusion-controlled mechanism may be more likely (Petrishcheva et al., 2019) for the development of these fine anastomosing networks of veinlets.

Significantly, there is a spatial and temporal association of a region of albite in the altered plagioclase where it intersects a prominent fracture which contains anhydrite and albite together with both bornite and chalcopyrite (Figure 20). Taking the primary plagioclase as An_{50}, this association is readily interpreted as being triggered by a gas-solid reaction of the form,

$$Ca_{0.5}Na_{0.5}Al_{1.5}Si_{2.5}O_{8(s)}+HCl+3H_2O \rightarrow 0.5NaAlSi_3O_{8(s)}+0.5CaCl_2+Al(OH)_3+H_4SiO_4 \quad (2)$$

Solid phases are here designated with the subscript (s) and for the purposes of illustration, reactions are written with reference to the dominant gas phase species for a given element; Ca for example is transported also as CaCl(OH) in magmatic gas mixtures (Henley and Fischer, 2021; Henley and Seward, 2018). Al and Si are dispersed with other gaseous species, into the connected porosity-fracture network. The transformation of andesine to albite results in a small (0.2%) decrease in volume that may be the source of some microporosity whose effect is to enable further gas permeation and release during alteration. The andesine conversion itself takes place as a sliding reaction as Ca is progressively removed to provide more albitic plagioclase. This is observed in the range of plagioclase analyses shown in Figure for samples G2 and G7.

Reaction 2 describes the solubility of andesine in the reactive gas mixture. Parallel solubility reactions occur for the alkali feldspars. For albite,

$$NaAlSi_3O_8 + HCl + 7H_2O \rightarrow \quad NaCl + Al(OH)_3 + 3H_4SiO_4 \quad (3)$$

$$KAlSi_3O_8 \; + \; HCl + 7H_2O \; \rightarrow \; KCl \; + Al(OH)_3 + 3H_4SiO_4 \quad (4)$$

The driving reaction for anhydrite-sulphide deposition in both vein and wallrock porosity may be written in the generalised form,

$$4CaCl_2 + 5SO_2 + 6H_2O \rightarrow 4CaSO_{4(s)} + 8HCl + H_2S + H_2 \quad (5)$$

The in-situ release of H_2S and H_2 then captures Cu and Fe from the oxidized magmatic gas stream (where, as shown in Table 7, $SO_2 >> H_2S$) to precipitate chalcopyrite and bornite. The efficiency of plagioclase to anhydrite reactions has been demonstrated experimentally elsewhere (Henley et al., 2015) with pure SO_2 gas over a temperature range of 500 to 800°C. These water-free experiments also demonstrated the nucleation and growth of an albitic region below the solid-gas interface, with associated aluminous material, below the interface with the gas phase.

A perennial concern in the replacement of plagioclase by alkali feldspar is the disposal of excess Al (Equation 2). The gas phase equilibrium solubility constants (K) for the alkali

feldspars (Equations 3 and 4) are low; for example, for both Na- and K-feldspar $K = 10^{-37}$ at 600°C. Exfiltration of excess $Al(OH)_3$ from the host rock into the fracture flow disturbs these solubility relations and this leads to supersaturation with respect to the alkali feldspar-gas equilibria and progressive infilling of the fracture with alkali feldspars simultaneously with anhydrite and Cu-Fe-sulphide as is evident in Figures 5 and 6. As an open system the evolved gas phase discharges into the general flux through the fractured porous medium. Infilling of the K-feldspar-anhydrite-sulphide vein indicates mass transfer from the wallrock and in turn this relates to the maintenance of connected microporosity. Equivalent dissolution occurs for magmatic biotite as it alters toward more phlogopitic composition releasing K and Fe into the gas phase. The specific association of sulphide mineralisation with alkali feldspar deposition appears to have been overlooked in reviews of porphyry copper mineralisation where a focus has been on a possible spatial association of sulphides directly with quartz veining.

Similar chemical processes dominated by anhydrite deposition also drove mineralisation skarn deposits such as Ertsberg, a younger mineralised system immediately adjacent to the Grasberg deposit (Henley et al., 2017; Sieber et al., 2020). Here other primary calcic phases, such as calcite and calcic garnet, react with SO_2 and HCl with the coupled deposition of metal sulphides.

Reference is made above to *equilibrium* solubilities. This is for convenience only, given that the alteration system is open at all scales. This has the effect of driving solubility reactions to the product side due to discharge of the evolved gas mixture, and similarly influx of HCl drives reactions to the product side. The same applies to the dissolution of the Ca-component of the primary plagioclase through deposition of very low solubility anhydrite. As a general observation, the mineral relations seen in these samples, such as the proximity of vein anhydrite and sulphides to albitised plagioclase do suggest that an assumption of equilibrium is reasonable even though the system is open to influx of magmatic gas and outflux of evolved gas mixtures. We note also that a further corollary of the model developed here is that $\Sigma K/\Sigma HCl$ in the gas phase is low, as it is in fumarole condensates (Henley and Seward, 2018). This contrasts with the much higher ratios that have been defined experimentally using liquid brines by Hemley and Jones (1964) who also recognized the role of HCl in driving potassium silicate alteration.

There are of course limits to the applicability of any closed system equilibrium modelling but these are beyond the scope of this paper. Some exploration of this field has been undertaken elsewhere by Henley and Berger (2000) and Ord et al. (2012) in terms of dissipative structures based on relative diffusion and reaction rates (Scott, 1991).

5.5. Other porphyry copper deposits

It has been shown above that the mineralogical and geochemical data from drillcore to mine scale at Grasberg may be integrated, through reasonable estimates of alteration depth and pressure, to provide a *quasi-isochemical model* for the major elements involved in potassium silicate rock alteration. The model, which is underpinned by thermochemical modelling (Henley and Fischer, 2021), is applicable to a majority of porphyry copper-gold deposits worldwide where anhydrite is a common gangue mineral. Some exceptions may be due to post-mineralisation dissolution of anhydrite or to replacement of anhydrite by epidote, analcite and sometimes calcite due to retrograde infiltration of groundwater. The importance of anhydrite formation in driving potassium silicate alteration in porphyry copper deposits has been

overlooked even though the abundance of anhydrite was well known to earlier workers (Burnham, 1962; Meyer and Hemley, 1967). This largely relates to a paradox arising from alteration petrography studies of the earliest developed porphyry copper deposits in the SW United States where anhydrite appeared to be almost absent. A prime example is Bingham Canyon, Utah, where potassium silicate alteration is well developed but anhydrite is not present above a quite considerable depth in the deposit as demonstrated by recent drilling (c.f. Appendix data in Henley et al. 2015). Anhydrite is, however, present with sulphides in the deep core of the more recently explored deposit at Resolution, Arizona (Hehnke et al., 2012) and in these and other deposits in the region fluid inclusion data show that the trapped liquid was anhydrite-supersaturated. Notably, at Bingham Canyon, Baumgartner et al. (1997) demonstrated at the mine scale the deficit in calcium that potentially results from low temperature dissolution and removal of soluble calcic alteration minerals such as anhydrite. Both at Resolution and at Grasberg, evidence has been obtained suggesting that such anhydrite removal is common during post-mineralisation influx by groundwater (Hehnke et al., 2012; Leys et al., 2020) as a result of its inverse liquid water solubility with respect to temperature.

While maar sediments and tuffs are preserved and mark the paleosurface at Grasberg during its formation, in most porphyry copper deposits their contemporary volcanic edifice has been eroded completely (Sillitoe, 1973). Exceptions include Cerro de Pasco (Peru) where mineralised clasts indicate an underlying porphyry copper system with fluid inclusion temperatures > 600 °C (Rottier et al., 2018; Rottier et al., 2020) and Cerro Colorado (Chile) (Bouzari and Clark, 2006). Near-surface alteration in such volcanic settings occurs around active fumarolic vents (Africano and Bernard, 2000) and, more extensively, where acidic gases (SO_2, HCl) are adsorbed into shallow, often perched, groundwater aquifers. This leads to intense alteration to sulphate-quartz-clay assemblages with dispersed, sometimes economic, deposition of Au-Ag-As ‘high sulphidation’ deposits (Berger and Henley, 2011; Henley and Berger, 2011) and sometimes extensive masses of native sulphur, as in the active White Island (New Zealand) volcano (Kilgour et al., 2021) and the 0.4 to 0.98 Ma Onto deposit in Sumbawa, Indonesia (Burrows et al., 2020). These assemblages are generally chemically unstable and structurally weak so that they erode away very quickly in regions of relatively high relief and high rainfall, eventually exposing the deeper potassic-altered regions that were developed as magmatic gas actively fluxed through the volcano. A feature of potassic (K-feldspar normative) altered rocks is that they are quite dense and hard due to their interlocking, fine-grained feldspar texture so that these may explain the deep resistive masses observed in resistivity surveys of active volcanoes. Surrounding lower resistivity rocks may then correlate with phyllic alteration containing clays, and secondary or retrograde chloritic clay. The continuum gas phase itself is not conductive, so that the conductivity of these rocks may be enhanced by networks of thin films of highly saline liquid condensate derived from magmatic gas expansion as determined from porphyry copper fluid inclusion studies (Mernagh et al., 2020) rather than more continuous lenses of brine as suggested by some authors (Blundy et al., 2021). The conductivity effect due to thin saline films in porous media has been documented elsewhere (Knackstedt et al., 2007).

6 Conclusions

Porphyry copper-gold deposits form within magmatic vapour plumes that are dominated by a continuum of high temperature gas containing highly reactive SO_2 and HCl along with Cu and other metals(Henley and McNabb, 1978; Mernagh et al., 2020; Weis et al., 2012). The continuum gas phase has only minor, < 2 volume percent, of saline liquid that separates by condensation during its expansion from source to surface. The permeability of plumes during porphyry copper evolution is maintained through their evolution by time variant internal and regional deviatoric stress.

Porphyry copper deposits are characterized by potassium silicate alteration, at the scale of several km^3 (Gustafson and Hunt, 1975; John et al., 2010; Lowell and Guilbert, 1970). This potassium silicate alteration is directly associated with Cu-Fe-S mineralisation and occurs in the giant 3.2 Ma Grasberg deposit (Indonesia) and elsewhere as a core of *potassic*, K-feldspar- and biotite-rich, assemblages surrounded by *phyllic*, mixed layer potassium phyllosilicates assemblages that pervasively replace the primary host rocks (Figures 2 and 3). Fluid inclusions in such assemblages have commonly been interpreted as due to deposit scale, potassium enrichment resulting from infiltration of a potassium-rich brine of unknown origin but which is commonly assumed to be a potassium-enriched magmatic vapour. However here we report detailed geochemical and petrographic data from the giant Grasberg porphyry copper-gold deposit (Indonesia) that disputes such interpretation.

The new data from Grasberg may be interpreted as showing, for the first time, that alteration at the deposit scale of several km^3 was essentially isochemical for the major rock forming elements Ca, K, Na, Al, Si and Fe. Only minor losses of these elements occur in the reactive magmatic gas phase as it expands and escapes to the surface regime of the deposit. There is no evidence at Grasberg for the involvement of a K-rich brine or K-enriched magmatic gas phase. Apparent potassium enrichment is the result of sequestration of calcium into anhydrite which with coupled sulphide formation requires that the alkali content of the remaining silicate sub-assemblage increases. It is this simple segregation that results in potassium silicate alteration. We have also shown how this alteration process continually evolves intergranular porosity during mineral replacement with secondary minerals, including anhydrite and sulphides, infilling porosity as it develops. In this way reactive gas flux is maintained in the altering host rock and sustained through higher flux of magmatic gas through developing fracture veins

These data underpin the development of a *quasi-isochemical* hypothesis for potassic alteration in porphyry copper deposits based on introduction of Cu and other metals with SO_2 and HCl, two of the common components of volcanic gases. A corollary is that such alteration is the normal process that occur to various extents in evolving magmatic arc volcanoes due to sub-surface gas-solid reactions. The correlation of porphyry copper formation with processes inside active volcanoes does not however mean that all alkali or calc-alkaline volcanoes, past and present, are host to porphyry copper formation. Their relative economic potential arises primarily from the relative fertility, with respect to copper, of the magmatic source regime that sustains an active volcano.

Acknowledgments

We wish to acknowledge the fundamental contributions made to the study of porphyry copper alteration by Charles Meyer, Julian Hemley, Lew Gustafson, Wayne Burnham and many other pioneers. Our thanks also go to PT Freeport Indonesia for provision of sample

suites and data. Andrew Putnis provided valuable discussion of replacement mechanisms and Dan Wood kindly provided helpful perspectives gained in several decades of porphyry copper exploration. We are also grateful for the comments provided by the reviewers of this paper and the constructive editorial suggestions from Tobias Fischer.

References

Africano, F. and Bernard, A., 2000. Acid alteration in the fumarolic environment of Usu volcano, Hokkaido, Japan. Journal of Volcanology and Geothermal Research, 97(1): 475-495.

Amiri, A., Ingram, G.D., Bekker, A.V., Livk, I. and Maynard, N.E., 2013. A multi-stage, multi-reaction shrinking core model for self-inhibiting gas–solid reactions. Advanced Powder Technology, 24(4): 728-736.

Andersen, P. and Evje, S., 2016. A model for reactive flow in fractured porous media. Chemical Engineering Science, 145: 196-213.

Anderson, G.M. and Crerar, D.A., 1993. Thermodynamics in geochemistry: The equilibrium model. Oxford University Press.

Arculus, R.J., 2003. Use and abuse of the terms calcalkaline and calcalkalic. Journal of Petrology, 44(5): 929-935.

Atkinson, W. W., Souviron, A., Vehrs, T.I., and Faunes, A., 1998. Geology and mineral zoning of the Los Pelambres porphyry copper deposit, Chile. Economic Geology, 73, 1326-1365.

Audétat, A., 2019. The Metal Content of Magmatic-Hydrothermal Fluids and Its Relationship to Mineralization Potential. Economic Geology 114, 1033–1056

Baumgartner, L.P., Gerdes, M.L., Person, M.A. and Roselle, G.T., 1997. Porosity and permeability of carbonate rocks during contact metamorphism, Fluid Flow and Transport in Rocks. Springer, pp. 83-98.

Bain, W.M., Lecumberri-Sanchez, P., Marsh, E.E., Steele-MacInnis, M., 2022. Fluids and Melts at the Magmatic-Hydrothermal Transition, Recorded by Unidirectional Solidification Textures at Saginaw Hill, Arizona, USA. Economic Geology 117, 1543–1571.

Beane, R., 1982. Hydrothermal alteration in silicate rocks. Advances in geology of the porphyry copper deposits, southwestern North America. The University of Arizona Press, Tucson, 117-137.

Berger, B.R. and Henley, R.W., 2011. Magmatic-vapor expansion and the formation of high-sulfidation gold deposits: Structural controls on hydrothermal alteration and ore mineralization. Ore Geology Reviews, 39(1): 75-90.

Berger, B.R. and Henley, R.W., 2011. Magmatic-vapor expansion and the formation of high-sulfidation gold deposits: Structural controls on hydrothermal alteration and ore mineralization. Ore Geology Reviews, 39(1-2), 75-90.

Berger, B.R., Henley, R.W., Lowers, H.A. and Pribil, M.J., 2014. The Lepanto Cu–Au deposit, Philippines: A fossil hyperacidic volcanic lake complex. Journal of Volcanology and Geothermal Research, 271, 70-82.

Berre, I., Doster, F. and Keilegavlen, E., 2019. Flow in fractured porous media: a review of conceptual models and discretization approaches. Transport in Porous Media, 130(1): 215-236.

Blundy, J., Afanasyev, A., Tattitch, B., Sparks, S., Melnik, O., Utkin, I. and Rust, A., 2021. The economic potential of metalliferous sub-volcanic brines. Royal Society Open Science, 8(6): 202192.

Bouzari, F. and Clark, A.H., 2006. Prograde evolution and geothermal affinities of a major porphyry copper deposit: the Cerro Colorado hypogene protore, I Región, northern Chile. Economic Geology, 101(1): 95-134.

Bruker, A.G., 2004. DiffracPlus Eva software version 10.0, Kahlruhr.

Burnham, C.W., 1962. Facies and types of hydrothermal alteration. Economic Geology, 57(5): 768-784.

Burrows, D.R., Rennison, M., Burt, D. and Davies, R., 2020. The Onto Cu-Au Discovery, Eastern Sumbawa, Indonesia: A Large, Middle Pleistocene Lithocap-Hosted High-Sulfidation Covellite-Pyrite Porphyry Deposit. Economic Geology, 115(7): 1385-1412.

Cardew, P. and Davey, R., 1985. The kinetics of solvent-mediated phase transformations. Proceedings of the Royal Society of London, A. Mathematical and Physical Sciences, 398(1815): 415-428.

Carten, R.B., Geraghty, E.P., Waqlker, B.M., Shannon, J.R., 1988. Cyclic Development of Igneous Features and Their Relationship to High-Temperature Hydrothermal Features in the Henderson Porphyry Molybdenum Deposit, Colorado. Economic Geology 83, 266-296.

Chiaradia, M. and Caricchi, L., 2022. Supergiant porphyry copper deposits are failed large eruptions. Communications Earth & Environment, 3(1): 1-9.

Chouinard, A., Williams-Jones, A.E., Leonardson, R.W., Hodgson, C.J., Silva, P., Tellez, J.V., Rojas, F., 2005. Geology and genesis of the multistage high-sulfidation epithermal Pascua Au–Ag–Cu deposit, Chile and Argentina. Economic Geology, 100, 463–490.

Cox, S., 2010. The application of failure mode diagrams for exploring the roles of fluid pressure and stress states in controlling styles of fracture- controlled permeability enhancement in faults and shear zones. Geofluids, 10(1- 2): 217-233.

Creasey, S.C., 1959. Some phase relations in the hydrothermally altered rocks of porphyry copper deposits. Economic Geology, 54(3): 351-373.

Crerar, D., Wood, S., Brantley, S. and Bocarsly, A., 1985. Chemical controls on solubility of ore-forming minerals in hydrothermal solutions. Canadian Mineralogist, 23(3): 333-352.

Data, I.C.F.D., 2004. ICDD (2004). PDF-2, Newtown Square, PA.

Deyell, C.L., Bissig, T., Rye, R.O., 2004. Isotopic evidence for magmatic-dominated epithermal processes in the El Indio-Pascua Au–Cu–Ag Belt and relationship to geomorphologic setting. Society of Economic Geologists Special Publication 11, 55–73.

Fogden, A., Middleton, J., McKay, T., Latham, S., Marathe, R., Turner, M., Sheppard, A., Howard, J. and Lane, F., 2014. 3D mapping of pore and organic matter distribution in unconventional reservoirs utilizing a digital rocks approach, International Symposium of the Society of Core Analysts, pp. 8-11.

Frank, M.R. and Vaccaro, D.M., 2012. An experimental study of high temperature potassic alteration. Geochimica et Cosmochimica Acta, 83: 195-204.

Garbe, U., Randall, T., Hughes, C., Davidson, G., Pangelis, S. and Kennedy, S., 2015. A new neutron radiography/tomography/imaging station DINGO at OPAL. Physics Procedia, 69: 27-32.

Gardner, J., Wheeler, J. and Mariani, E., 2021. Interactions between deformation and dissolution-precipitation reactions in plagioclase feldspar at greenschist facies. Lithos, 396: 106241.

Glassley, W.E., Simmons, A.M. and Kercher, J.R., 2002. Mineralogical heterogeneity in fractured, porous media and its representation in reactive transport models. Applied Geochemistry, 17(6): 699-708.

Golab, A.N., Knackstedt, M.A., Averdunk, H., Senden, T., Butcher, A.R. and Jaime, P., 2010. 3D porosity and mineralogy characterization in tight gas sandstones. The leading edge, 29(12): 1476-1483.

Grant, J.A., 1986. The isocon diagram; a simple solution to Gresens' equation for metasomatic alteration. Economic geology, 81(8): 1976-1982.

Gustafson, L.B. and Hunt, J.P., 1975. The porphyry copper deposit at El Salvador, Chile. Economic Geology, 70: 857-912.

Gustafson, L. B., and Quiroga, J., 1995. Patterns of Mineralization and Alteration below the Porphyry Copper Orebody at El Salvador, Chile. Economic Geology, 90, 2-16.

Harris, A.C., Kamenetsky, V.S., White, N.C. and Steele, D.A., 2004. Volatile phase separation in silicic magmas at Bajo de la Alumbrera porphyry Cu- Au deposit, NW Argentina. Resource Geology, 54(3): 341-356.

Harrison, J.S., 1999. Hydrothermal alteration and fluid evolution of the Grasberg porphyry Cu-Au deposit, Irian Jaya, Indonesia, University of texas at Austin, 205 pp.

Hedenquist, J. W., & Henley, R. W. (1985). The importance of CO 2 on freezing point measurements of fluid inclusions; evidence from active geothermal systems and implications for epithermal ore deposition. *Economic geology*, *80*(5), 1379-1406.

Hehnke, C., Ballantyne, G., Martin, H., Hart, W., Schwartz, A. and Stein, H., 2012. Geology and Exploration progress at the Resolution porphyry Cu-Mo deposit, Geology and genesis of major copper deposits and districts of the world. Society of Economic Geologists, pp. 147-166.

Hemley, J.J. and Jones, W., 1964. Chemical aspects of hydrothermal alteration with emphasis on hydrogen metasomatism. Economic Geology, 59(4): 538-569.

Henley, R.W., 2015. Hyperacidic volcanic lakes, metal sinks and magmatic gas expansion in arc volcanoes. In Rouwet, D., Christenson, B., Tassi, F. and Vandemeulebrouck, J. (Eds), Volcanic Lakes. Springer, Berlin, Heidelberg, pp. 155-178.

Henley, R. W., and Berger, B.R., 2000. Self-ordering and complexity in epizonal mineral deposits. Annual Review of Earth and Planetary Sciences, 28, 669-719.

Henley, R.W. and Berger, B.R., 2011. Magmatic-vapor expansion and the formation of high-sulfidation gold deposits: Chemical controls on alteration and mineralization. Ore Geology Reviews, 39(1): 63-74.

Henley, R.W. and Berger, B.R., 2012. Pyrite–sulfosalt reactions and semimetal fractionation in the Chinkuashih, Taiwan, copper–gold deposit: a 1 Ma paleo-fumarole. Geofluids, 12(3), pp.245-260.

Henley, R.W. and Berger, B.R., 2013. Nature's refineries — Metals and metalloids in arc volcanoes. Earth-Science Reviews, 125: 146-170.

Henley, R.W., Brink, F.J., King, P.L., Leys, C., Ganguly, J., Mernagh, T., Middleton, J., Renggli, C.J., Sieber, M. and Troitzsch, U., 2017. High temperature gas–solid reactions in calc–silicate Cu–Au skarn formation; Ertsberg, Papua Province, Indonesia. Contributions to Mineralogy and Petrology, 172(11-12): 106.

Henley, R.W. and Ellis, A.J., 1983. Geothermal systems ancient and modern: a geochemical review. Earth-Science Reviews, 19(1): 1-50.

Henley, R.W. and Fischer, T.P., 2021. Sulfur sequestration and redox equilibria in volcanic gases. Journal of Volcanology and Geothermal Research.

Henley, R.W. and Hughes, G.O., 2016. SO 2 flux and the thermal power of volcanic eruptions. Journal of Volcanology and Geothermal Research: 190-199.

Henley, R.W., King, P.L., Wykes, J.L., Renggli, C.J., Brink, F.J., Clark, D.A. and Troitzsch, U., 2015. Porphyry copper deposit formation by sub-volcanic sulphur dioxide flux and chemisorption. Nature Geoscience, 8(3): 210-215.

Henley, R.W. and McNabb, A., 1978. Magmatic vapor plumes and ground-water interaction in porphyry copper emplacement. Economic Geology, 73(1): 1-20.

Henley, R.W. and Seward, T.M., 2018. Gas-Solid Reactions in Arc Volcanoes; Ancient and Modern. Reviews in Mineralogy and Geochemistry, 84: 309-350.

Hövelmann, J., Putnis, A., Geisler, T., Schmidt, B.C. and Golla-Schindler, U., 2010. The replacement of plagioclase feldspars by albite: observations from hydrothermal experiments. Contributions to Mineralogy and Petrology, 159(1): 43-59.

Hurtig, N.C., Migdisov, A.A. and Williams-Jones, A.E., 2021. Are Vapor-Like Fluids Viable Ore Fluids for Cu-Au-Mo Porphyry Ore Formation? Economic Geology, 116(7),1599-1624.

IUPAC, 2014. Compendium of Chemical Terminology, 1670 pp.

Jacobs, D. and Parry, W.T., 1979. Geochemistry of biotite in the Santa Rita porphyry copper deposit, New Mexico. Economic Geology, 74(4): 860-887.

John, D.A., Ayuso, R., Barton, M., Blakely, R., Bodnar, R., Dilles, J., Gray, F., Graybeal, F., Mars, J. and McPhee, D., 2010. Porphyry copper deposit model. Chapter B of Mineral deposit models for resource assessment: US Geological Survey Scientific Investigations Report: 169.

Kerrick, D., 1972. Experimental determination of muscovite+ quartz stability with P H2O< P total. American Journal of Science, 272(10): 946-958.

Kilgour, G., Kennedy, B., Scott, B., Christenson, B., Jolly, A., Asher, C., Rosenberg, M. and Saunders, K., 2021. Whakaari/White Island: a review of New Zealand's most active volcano. New Zealand Journal of Geology and Geophysics, 64(2-3): 273-295.

Kingston, A., Sakellariou, A., Varslot, T., Myers, G. and Sheppard, A., 2011. Reliable automatic alignment of tomographic projection data by passive auto- focus. Medical physics, 38(9): 4934-4945.

Knackstedt, M. A., Arns, C. H., Sheppard, A. P., Senden T. J., Sok R. M., Cinar, Y., Olafuyi, A. O., Pinczewski, W.V., Padhy, G., and Ioannidis M., 2007. Pore scale analysis of electrical resistivity in complex core material. Proc. of the Soc. Core Analysts, Calgary, Canada. SCA2007-33, 1-12.

Kouzmanov, K., and Pokrovski, G.S., 2012. Hydrothermal Controls on Metal Distribution in Porphyry Cu (-Mo-Au) Systems. Society of Economic Geologists, Inc. Special Publication 16, 573–618.

Kubicki, J.D. and Watts, H.D., 2018. Reaction Mechanisms and Solid-Gas Phase Reactions: Theory and Density Functional Theory Simulations. Reviews in Mineralogy and Geochemistry, 84: 85-102.

Latham, S., Varslot, T. and Sheppard, A., 2008. Image registration: enhancing and calibrating X-ray micro-CT imaging. Proc. of the Soc. Core Analysts, Abu Dhabi, UAE: 1-12.

Lerchbaumer, L. and Audétat, A., 2012. High Cu concentrations in vapor-type fluid inclusions: An artifact? Geochimica et Cosmochimica Acta, 88: 255-274.

Leys, C., Schwarz, A., Cloos, M., Widodo, S., Kyle, J.R. and Sirait, J., 2020. Grasberg Copper-Gold-(Molybdenum) Deposit: Product of Two overlapping Porphyry Systems. In: R.H. Sillitoe, R. Goldfarb, J, F. Robert and S. Simmons, F (Editors), Geology of the World's Major Gold Deposits and Provinces. Society of Economic Geologists, pp. 599-620.

Leys, C.A., Cloos, M., New, B.T. and MacDonald, G.D., 2012. Copper-gold±molybdenum deposits of the Ertsberg-Grasberg District. Papua, Indonesia: Society of Economic Geologists, Special Publication, 16: 215-235.

Limaye, A., 2012. Drishti: a volume exploration and presentation tool. Proc Spie, 8506: 85060X-85060X.

Lowell, J.D. and Guilbert, J.M., 1970. Lateral and vertical alteration-mineralization zoning in porphyry ore deposits. Economic geology, 65(4): 373-408.

Lortie, R.B. and Clark, A.H., 1987. Strata-bound cupriferous sulfide mineralization associated with continental rhyolitic volcanic rocks, northern Chile; I, The Jardin copper-silver deposit. Economic Geology, *82*(3), 546-570.

MacDonald, G.D. and Arnold, L.C., 1994. Geological and geochemical zoning of the Grasberg igneous complex, Irian Jaya, Indonesia. Journal of Geochemical Exploration, 50(1): 143-178.

Mernagh, T.P., Leys, C. and Henley, R.W., 2020. Fluid inclusion systematics in porphyry copper deposits: the super-giant Grasberg deposit, Indonesia, as a case study. Ore Geology Reviews: 103570.

Mernagh, T.P. and Mavrogenes, J., 2019. Significance of high temperature fluids and melts in the Grasberg porphyry copper‐gold deposit. Chemical Geology, 508: 210-224.

Meyer, C. and Hemley, J.J., 1967. Wall rock alteration. In: H.L. Barnes (Editor), Geochemistry of Hydrothermal Ore Deposits. Holt, Rinehart and Winston, Inc., pp. 166-235.

Nadeau, O., Stix, J. and Williams-Jones, A.E., 2016. Links between arc volcanoes and porphyry-epithermal ore deposits. Geology, 44(1): 11-14.

Niedermeier, D.R., Putnis, A., Geisler, T., Golla-Schindler, U. and Putnis, C.V., 2009. The mechanism of cation and oxygen isotope exchange in alkali feldspars under hydrothermal conditions. Contributions to Mineralogy and Petrology, 157(1): 65-76.

Norton, D. and Knapp, R., 1977. Transport phenomena in hydrothermal systems: the nature of porosity. Am. J. Sci.;(United States), 277.

Ord, A., Hobbs, B.E. and Lester, D.R., 2012. The mechanics of hydrothermal systems: I. Ore systems as chemical reactors. Ore Geology Reviews, 49, 1-44.

Park, J.W., Campbell, I.H., Chiaradia, M., Hao, H. and Lee, C.-T., 2021. Crustal magmatic controls on the formation of porphyry copper deposits. Nature Reviews Earth & Environment, 2(8): 542-557.

Parry, W., Jasumback, M. and Wilson, P.N., 2002. Clay mineralogy of phyllic and intermediate argillic alteration at Bingham, Utah. Economic Geology, 97(2): 221-239.

Paterson, J.T., 2004. Magmatic and Pervasive Hydrothermal Mineralogy of the Grasberg Cu-Au Porphyry Copper Deposit (West New Guinea), MSc Thesis, University of Texas at Austin, 348 pp.

Paterson, J.T. and Cloos, M., 2005a. Grasberg porphyry Cu–Au deposit, Papua, Indonesia: 1. Magmatic history. In: P. TM (Editor), Super porphyry copper and gold deposits: A global perspective: Adelaide. PGC Publishing, South Australia, 313-330 pp.

Paterson, J.T. and Cloos, M., 2005b. Grasberg porphyry Cu–Au deposit, Papua, Indonesia: 2. Pervasive hydrothermal alteration. In: P. TM (Editor), Super porphyry copper and gold deposits: A global perspective: Adelaide. PGC Publishing, South Australia, 331-356.

Penniston-Dorland, S.C., 1997. Veins and Alteration Envelopes in the Grasberg Igneous Complex, Gunung Bijih (Ertsberg) District, Irian Jaya, Indonesia, University of Texas at Austin. 402pp.

Petrishcheva, E., Rieder, M., Predan, J., Fischer, F.D., Giester, G. and Abart, R., 2019. Diffusion-controlled crack propagation in alkali feldspar. Physics and chemistry of minerals, 46(1): 15-26.
Petrishcheva, E., Tiede, L., Heuser, D., Hutter, H., Giester, G. and Abart, R., 2020. Multicomponent diffusion in ionic crystals: theoretical model and application to combined tracer-and interdiffusion in alkali feldspar. Physics and chemistry of minerals, 47(8): 1-10.
Pollard, P.J. and Taylor, R.G., 2002. Paragenesis of the Grasberg Cu–Au deposit, Irian Jaya, Indonesia: results from logging section 13. Mineralium Deposita, 37(1): 117-136.
Pouchou, J., Pichoir, F.I., Heinrich, K. and Newbury, D., 1991. Electron probe quantitation. Plenum Press.
Putnis, A., 2009. Mineral Replacement Reactions. Reviews in Mineralogy and Geochemistry, 70(1): 87-124.
Putnis, A., 2021. Fluid–Mineral Interactions: Controlling Coupled Mechanisms of Reaction, Mass Transfer and Deformation. Journal of Petrology, 62(12): egab092.
Putnis, A. and Putnis, C.V., 2007. The mechanism of reequilibration of solids in the presence of a fluid phase. Journal of Solid State Chemistry, 180(5): 1783-1786.
Ravi-Chandar, K. and Knauss, W., 1984. An experimental investigation into dynamic fracture: II. Microstructural aspects. International Journal of Fracture, 26(1): 65-80.
Redmond, P.B. and Einaudi, M.T., 2010. The Bingham Canyon porphyry Cu-Mo-Au deposit. I. Sequence of intrusions, vein formation, and sulfide deposition. Economic Geology, 105(1): 43-68.
Reyes, A.G., 1990. Petrology of Philippine geothermal systems and the application of alteration mineralogy to their assessment. Journal of Volcanology and geothermal research, 43(1-4): 279-309. Rottier, B., Kouzmanov, K., Casanova, V., Bouvier, A.S., Baumgartner, L.P., Wälle, M. and Fontboté, L., 2018. Mineralized breccia clasts: a window into hidden porphyry-type mineralization underlying the epithermal polymetallic deposit of Cerro de Pasco (Peru). Mineralium Deposita, 53(7): 919-946.
Rottier, B., Kouzmanov, K., Ovtcharova, M., Ulianov, A., Wälle, M., Selby, D. and Fontboté, L., 2020. Multiple rejuvenation episodes of a silicic magma reservoir at the origin of the large diatreme-dome complex and porphyry-type mineralization events at Cerro de Pasco (Peru). Lithos, 376: 105766.
Sapiie, B. and Cloos, M., 2004. Strike-slip faulting in the core of the Central Range of west New Guinea: Ertsberg Mining District, Indonesia. Geological Society of America Bulletin, 116(3-4): 277-293.
Scott, S. K. 1993. Chemical Chaos. Oxford University Press, 454 pp.
Sheppard, A.P., Sok, R.M. and Averdunk, H., 2004. Techniques for image enhancement and segmentation of tomographic images of porous materials. Physica A: Statistical mechanics and its applications, 339(1): 145-151.
Sieber, M., Brink, F.J., Leys, C., King, P.L. and Henley, R.W., 2020. Prograde and retrograde metasomatic reactions in mineralised magnesium-silicate skarn in the Cu-Au Ertsberg East Skarn System, Ertsberg, Papua Province, Indonesia. Ore Geology Reviews, 125: 103697, 1-14.
Sillitoe, R.H., 1973. The tops and bottoms of porphyry copper deposits. Economic Geology, 68(6): 799-815.
Sillitoe, R.H., 2010. Porphyry copper systems. Economic geology, 105(1): 3-41.
Singer, D.A., 2017. Future copper resources. Ore Geology Reviews, 86: 271-279.
Smith, H.E., Bevitt, J.J., Zaim, J., Rizal, Y., Puspaningrum, M.R., Trihascaryo, A., Price, G.J., Webb, G.E. and Louys, J., 2021. High-resolution high-throughput thermal

neutron tomographic imaging of fossiliferous cave breccias from Sumatra. Scientific reports, 11(1): 1-16.

Steefel, C.I. and Atkinson, W.W., 1984. Hydrothermal andalusite and corundum in the Elkhorn district, Montana. Economic Geology, 79(3):573-579.

Sulaksono, A., Watanabe, Y., Arribas, A., Echigo, T., Al Furqan, R. and Leys, C.A., 2021. Reduction of oxidized sulfur in the formation of the Grasberg porphyry copper-gold deposit, Papua, Indonesia. Mineralium Deposita, 56(6): 1027-1042.

Ulrich, T., Gunther, D., Heinrich, C.A., 1999. Gold concentrations of magmatic brines and the metal budget of porphyry copper deposits. Nature 399: 676–679.

Varslot, T., Kingston, A., Myers, G. and Sheppard, A., 2011a. High-resolution helical cone-beam micro-CT with theoretically-exact reconstruction from experimental data. Medical physics, 38(10): 5459-5476.

Varslot, T., Kingston, A., Myers, G. and Sheppard, A., 2011b. High- resolution helical cone- beam micro- CT with theoretically- exact reconstruction from experimental data. Medical physics, 38(10): 5459-5476.

Voisey, C.R., Willis, D., Tomkins, A.G., Wilson, C.J., Micklethwaite, S., Salvemini, F., Bougoure, J. and Rickard, W.D., 2020. Aseismic refinement of orogenic gold systems. Economic Geology, 115(1): 33-50.

Wahrenberger, C., 1997. Some aspects of the chemistry of volcanic gases, Swiss Federal Institute of Technology Zurich, Zurich, 235 pp.

Warr, L.N., 2018. A new collection of clay mineral 'Crystallinity'Index Standards and revised guidelines for the calibration of Kübler and Árkai indices. Clay Minerals, 53(3): 339-350.

Wagner, W. and Kretzschmar, H.J., 2008. IAPWS industrial formulation 1997 for the thermodynamic propoerties of water and steam. International Steam Tables: Properties of Water and Steam Based on the Industrial Formulation IAPWS-IF97, 7-150.

Watanabe, Y. and Hedenquist, J.W., 2001. Mineralogic and stable isotope zonation at the surface over the El Salvador porphyry copper deposit, Chile. Economic Geology, 96(8): 1775-1797.

Weis, P., Dreisner, T. and Heinrich, C.A., 2012. Porphyry-copper ore shells form at stable pressure-temperature fronts within dynamic fluid plumes. Science, 338: 1613-1616.

Williams, J.N., Bevitt, J.J. and Toy, V.G., 2017. A comparison of the use of X-ray and neutron tomographic core scanning techniques for drilling projects: insights from scanning core recovered during the Alpine Fault Deep Fault Drilling Project. Scientific Drilling, 22: 35-42.

Zelenski, Michael E., Fischer, T.P., De Moor, J.M., Marty, B., Zimmermann, L., Ayalew, D., Nekrasov, A.N. and Karandashev, V.K., 2013. Trace elements in the gas emissions from the Erta Ale volcano, Afar, Ethiopia. Chemical Geology, 357: 95-116.

Zhang, Y., Mostaghimi, P., Fogden, A., Middleton, J., Sheppard, A. and Armstrong, R.T., 2017. Local diffusion coefficient measurements in shale using dynamic micro-computed tomography. Fuel, 207: 312-322.

Zimmer, M.M., Plank, T., Hauri, E.H., Yogodzinski, G.M., Stelling, P., Larsen, J., Singer, B., Jicha, B., Mandeville, C. and Nye, C.J., 2010. The role of water in generating the calc-alkaline trend: new volatile data for Aleutian magmas and a new tholeiitic index. Journal of Petrology, 51(12): 2411-2444.

Figure 1. Location of the 3.3-3.6 Ma Grasberg porphyry copper deposit within a maar volcanic vent cutting through a Mesozoic carbonate-siliciclastic basement rock sequence (Leys et al., 2020; Leys et al., 2012).

Figure 2 Distribution of selected minerals and metals in a cross section of the Grasberg deposit relative to the estimated paleosurface as defined in Mernagh et al., (2020).

Figure 3 (a) Geology and b) alteration assemblage distribution on a SW-NE cross section through the Grasberg deposit showing the locations of the samples discussed in this paper. The alteration data, shown here in summary form, are discussed in detail by Leys et al. (2020). The distinct Heavy Sulphide zone adjacent to the diatreme margin is comprised of massive pyrite with variable amounts of chalcopyrite and minor covellite, sphalerite and enargite (Leys et al., 2020). The solid lines are the track of drill holes that were collared underground and for which the samples discussed in this paper were obtained. The general location of the open pit float sample is shown with reference to the base of the pit at the time of sampling. The dashed lines outline regions containing >1 wt% Cu. The approximate level of the paleosurface is shown based on the data of Mernagh et al. (2020)
.

Figure 4 Photographs of the potassium feldspar altered drillcore specimens used in this study. a) Dalam Diorite (Tgdd) or occluded block of this in Dalam Fragmental Andesite (Tgdfa). The sample is only partially altered and retains altered plagioclase feldspar and biotite phenocrysts and a K-feldspar-rich matrix as described in the text. Anhydrite with associated chalcopyite and bornite occurs as narrow veins and as disseminated clusters through the matrix, b) combined X-ray μCT and thermal neutron tomogram of sample G2, c) Intensely potassic-altered Dalam Fragmental Andesite showing K-feldspar (grey-mauve) and secondary biotite cut by quartz-anhydrite veining and associated chalcopyite and bornite, *d)* combined X-ray μCT and thermal neutron tomograph of sample G7, e) intense muscovite-quartz (phyllic) altered open pit sample containing pyrite and a vein with bornite (bn) and anhydrite (anh), and f) polished slab of GP from the wallrock adjacent to the anhydrite-sulphide vein. Sample locations are shown in Figure 3.

Figure 5. ™QEMSCAN mineral map for a cross section of the Dalam Diorite subcore (G2) showing the relative abundance of altered plagioclase and 'biotite' phenocrysts, through-going fractures and healed microfractures that are filled by anhydrite, chalcopyrite, bornite and K-feldspar with lesser albite. High resolution maps for specific sites of interest (SOI) areas 1 and 2 are shown in Figure and Figure 8. Only principal phases are shown and the full scan image is provided in the Supplement. Plagioclase solid solution is provided as a colour scale between labradorite and albite composition in the legend and note that the primary phenocryst composition is andesine.

Figure 6 a) High resolution mineral map of the area SOI 1 shown in Figure for sample G2. Note the specific association of Ca-depleted plagioclase (albite) with the vein margin adjacent to sulphide and anhydrite nucleation and growth in the vein. Anastomosing veinlets of albite penetrate across the phenocrysts. K-feldspar replacement of the phenocryst margin is evident together with anastomosing vein networks of K-feldspar through the phenocryst. There is void space along the vein margin that either are primary porosity remaining after vein formation ceased or, less likely plucking during polishing. b) Relative ternary ratios of Ca, Na and K element concentrations in area SOI 1. The element distributions demonstrate the nucleation and growth of albite adjacent to the fracture channel with release of Ca to nucleate vein anhydrite. The map also shows the concomitant dissolution and replacement of

the plagioclase by K-feldspar due to infiltrated K from the matrix and dissolution of biotite as discussed in the text.

Figure 7 Alteration feldspar compositions from samples G2 (area Y in Figure 6) and G7 in comparison with primary magmatic feldspar compositions at Grasberg (grey shaded area) from Paterson (2004).

Figure 8. Sample G2: High resolution mineral map of area SOI 2 (Figure 5) showing the replacement of primary biotite by phlogopitic biotite and K-feldspar.

Figure 9. Comparison of EDS spot analyses of the biotite phenocrysts in the area of interest SOI 2 of sample G2 (Figure 5) and in sample G7 (Figure 10).

Figure 10. a) High resolution QEM mineral map for sample G7. b) enlarged to show the margin of the pre-alteration quartz vein that is now fractured and infilled by anhydrite, sulphide and alkali feldspar. c) zoomed image to show the location of molybdenite(mo), other sulphides and corundum (crn).

Figure 11. a) ™QEMSCAN mineral map showing intense illite-quartz alteration in sample GP from the Grasberg open pit (Figure). The image shows the upper part of a 91mm long scan extending from an extensional vein of bornite-chalcopyrite-anhydrite into the altered Dalam host rock and towards another vein. Well-crystallized illite/muscovite (45.6 area %) pseudomorphically replaces primary plagioclase, biotite and horneblende, and quartz (37.9 area%) replaces the primary matrix. Chalcopyrite (2.2 area%), pyrite (1.1 area%) and anhydrite (8.3 area %) are disseminated as isolated grains and infilled microfractures through the wallrock. Minor phlogopite, apatite and rutile are present and there is residual biotite distal to the vein. No sodium is present in the illite. b) shows the polished slab of sample GP whose central section was scanned for the QEM mineral variety map shown in a), and c) is a zoomed in part of the full image that is several mm below a) and shows calcite and anhydrite occurring together: the full image is provided in the Supplement.

Figure 12. Distribution of microporosity in the feldspar assemblage across the plagioclase phenocryst margin in the region POR that is located in Figure . a-d are high resolution back scattered and secondary electron images of a part of this region. The inset shows part of the area segmented with the same colour legend as in Figure 6. Abbreviations: quartz, qz; K-feldspar,or; albite, ab; plagioclase, plag and phlogopite, phl.
.

Figure 13 a) Unsegmented X-ray μCT tomogram of subcore of G2 showing veins and the distribution of altered phenocrysts at a voxel resolution of 5.3 μm. b) 2D microporosity map of the X-ray μCT section equivalent to the mineral map shown in Figure 5**,** where blue registers regions of essentially no porosity (<1% voxel porosity), grey to black indicates regions of high voxel porosity 1 -10%, and red indicates regions of >10% voxel porosity. c) reproduces Figure 5 in order to provide reference for the microporosity slice of the subsample tomogram. Region 1 locates one of the altered plagioclase phenocrysts, regions marked 2 identify altered magmatic biotite and region 3 focusses on the matrix assemblage between phenocrysts.

Figure 14 Visualization of the G7 sample as a μCT tomogram slice (voxel resolution 5.3μm) showing the general texture of the rock matrix, fractured quartz veins with anhydrite and silicate fracture fill and Cu-Fe sulphides (c.f.Figure). a) and b) show the distribution of

microporosity using the same colour scheme as in Figure 13. The tomogram is for a lozenge-shaped sample from the cut slab adjacent to that shown in Figure 4.

Figure 15. Examples of fluid inclusion trapped in anhydrite from Grasberg. (a) Vapor-rich inclusions containing <20 vol% liquid, (b) Rare, liquid-rich inclusion with ~10 vol% vapor, (c) and (d) irregularly shaped, liquid + vapor inclusions with <30 vol% vapor. These inclusions did not freeze at temperatures as low as -180 C, which may indicate a $CaCl_2$ dominant aqueous phase.

Figure 16 Schematic showing the principal components of the hydrodynamics of a volcanic hydrothermal system in the context of formation of a major porphyry copper deposit associated with a maar volcano at Grasberg, Indonesia. The figure emphasizes the scales of magmatic vapour expansion (light grey gradient infill) to form the plume and the peripheral interactions with groundwater (Henley and McNabb 1978). The expansion path for magmatic fluid is cartooned in as the blue arrow and its expansion through the high permeability diatreme region shown figuratively as red arrows. The figure includes the outline (blue) of the Grasberg porphyry copper deposit, relative to its estimated paleo-surface, as described in the text.

Figure 17 Comparison of compositions of average phyllic and potassic K-feldspar altered rocks with the composition of weakly altered Dalam volcanic and intrusive host rocks. a) and b) show wt % analyses for the major rock forming oxide components in relation to the composition of Dalam host rocks as described in the text. c) provides the comparison of normalised water, Cu and S free potassic and phyllic altered rock compositions with the Dalam host rocks.

Figure 18. Ternary plots showing the relative distribution of primary rock compositions (purple) (normalised to anhydrous) and alteration minerals as described in the text.

Figure 19. Contoured enthalpy (blue) and entropy (black) data for pure water (Wagner and Kretzschmar, 2008). Shown in red is an isentropic expansion path for magmatic gas through the evolving Grasberg deposit, as discussed in the text, from lithostatic pressure within the water-undersaturated melt field of dacite(shaded) as determined by (Holtz, 2001) to the surface. The path illustrated is necessarily generalised and shown for the condition where the expanded gas phase has a pressure less than lithostatic and higher than that of external groundwater as described in the text. The open circles are the estimated pressure temperature locations for samples G2, G7 and GP along the illustrative expansion path. Thermodynamic data for water are a very good proxy for those of water-rich volcanic gas mixtures as discussed elsewhere (Mernagh et al., 2020).

Figure 20. a) illustrates the fluctuations of gas pressure in a fractured porous rock through several cycles of hydraulic fracture formation. It is these cycles that control permeation of the altering porous rock and egress of evolved gas mixtures into new and reopened fractures that results in coupled alteration and mineralisation. b) The schema shows input (yellow) of reactive magmatic gas containing Cu, Fe and other ore metals, through a fracture and relative flow paths through the high permeability fracture vein and microporous wallrock. Reacted gas outflux to the fracture is shown in white. Note that this flow schematic is very highly generalised and is for illustration purposes alone. Ca removal from plagioclase leads to anhydrite deposition in the fracture vein and macroporosity and sulphide formation. Alkali feldspar also deposits in the developing vein as shown in Figure 5 and discussed in the text.

1748 Output (red) includes excess Na, K, Cu, and sulphur species. For convenience the schema is
1749 illustrated using the Na-Ca-K element map provided in Figure 6.
1750

Table 1. Average whole rock analyses of variously altered Dalam stage rocks (MacDonald and Arnold, 1994) from a suite of 1400 outcrop and drillhole samples. The data were normalized after removal of the LOI and S in the original data (up to 5.5 and 3.8 wt %, respectively),

Table 2. Volumes of potassic and phyllic in the Grasberg porphyry copper deposit and their average mineral compositions based on proprietary XRD data kindly provided by P.T. Freeport Indonesia

Table 3. Upper and lower pressure, density and temperature limits for alteration processes for the 3 samples discussed in this paper

Table 4. Relative proportion of minerals (by area %) in the QEM mineral variety maps provided in Figure 5 and Figure 10 for samples G2 and G7. Mineral abundances above 0.5 volume percent. Note that plagioclase per cents report to the appropriate part of the plagioclase solid solution series for each sample with andesine dominating the plagioclase.

Table 5. a) Average major oxide compositions and standard deviations of potassic and phyllic altered rocks at Grasberg. The data have been recalculated water-free and normalized after removal of minor elements and of S and Cu as introduced elements. b) Major element compositions of least altered Dalam volcanic and intrusive rocks (Table 1) and the average altered rocks converted to atomic proportions and normalized to 3 oxygen atoms. The proprietary alteration composition data were kindly provided by P.T. Freeport Indonesia.

Table 6 . Reference magmatic gas phase composition. This representative gas analysis for arc volcanic systems is one that was sampled by Wahrenberger (1997) in a Kudryavy Volcano (Russia) fumarole at 920 °C and discussed further in terms of gas phase speciation and redox state by Henley and Seward (2018) and by Henley and Fischer (2021).

Table 7. Estimation of the minimum mass of water and water-rock ratio for the formation of the Grasberg porphyry copper deposit based on the average compositions of the phyllic and potassic altered rocks at the mine scale and the ratio of H_2O:SO_2 in a representative high temperature volcanic gas. Note that w/r is a minimum value since the calculation here assumes complete reaction; incomplete reaction would increase the time-integrated w/r.* The average of the w/r values for the two alteration zones.

Figure

Click here to access/download;Figure;Figure 1 regional map.tif

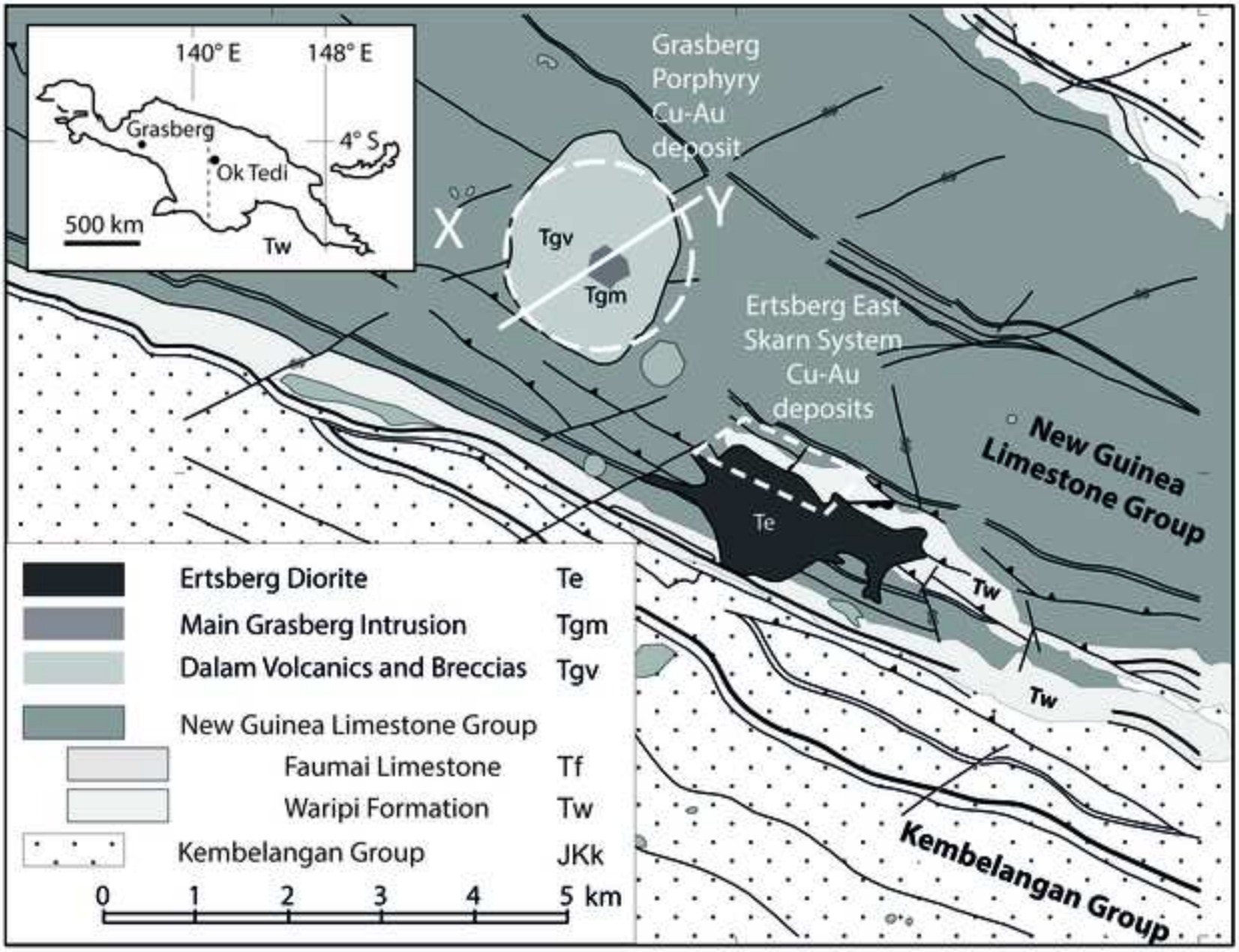

Figure

Click here to access/download;Figure;Figure 2 alteration mineral section composite.tif

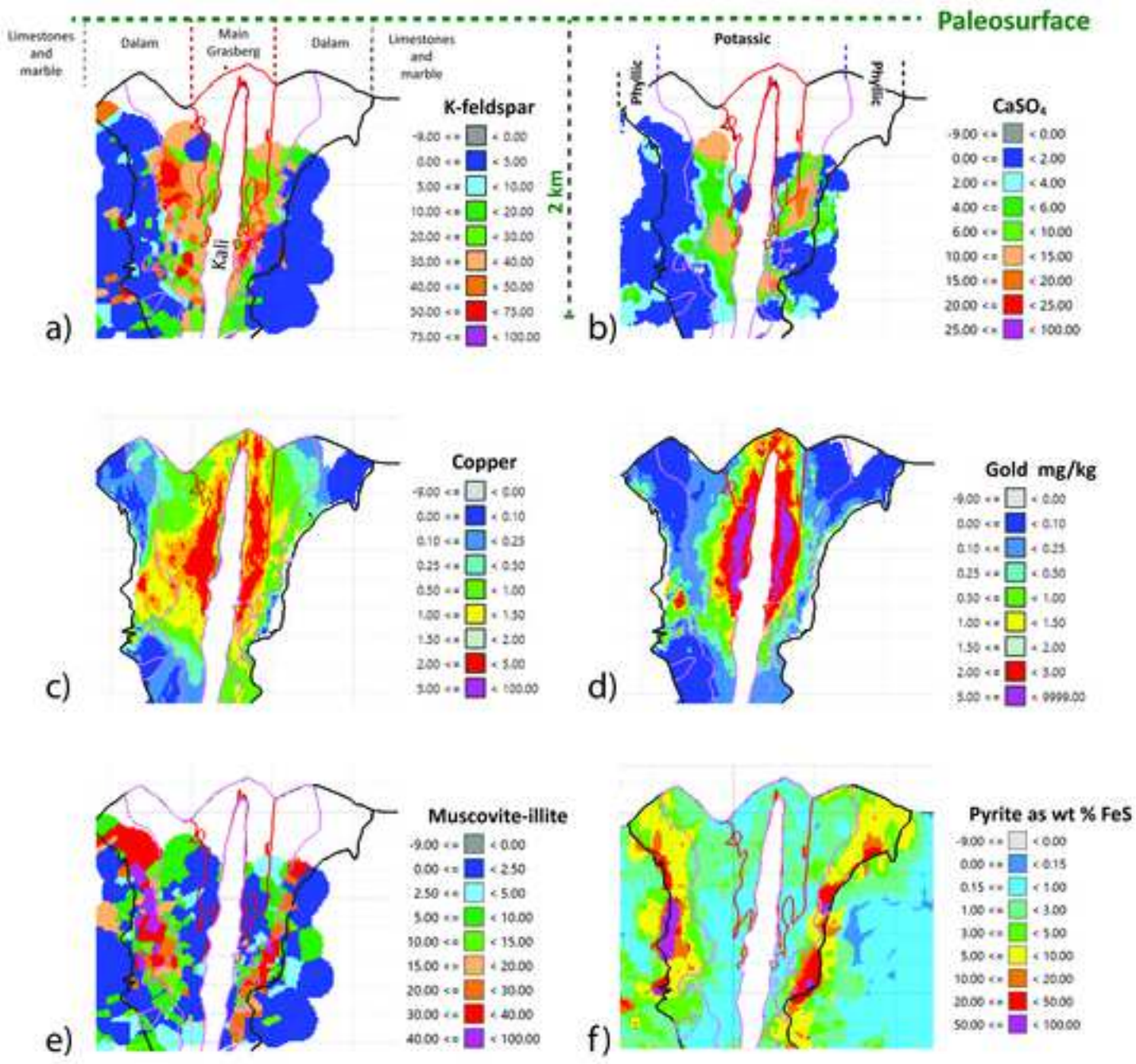

Figure

Click here to access/download;Figure;Figure 3 geology and alteration sections.tif

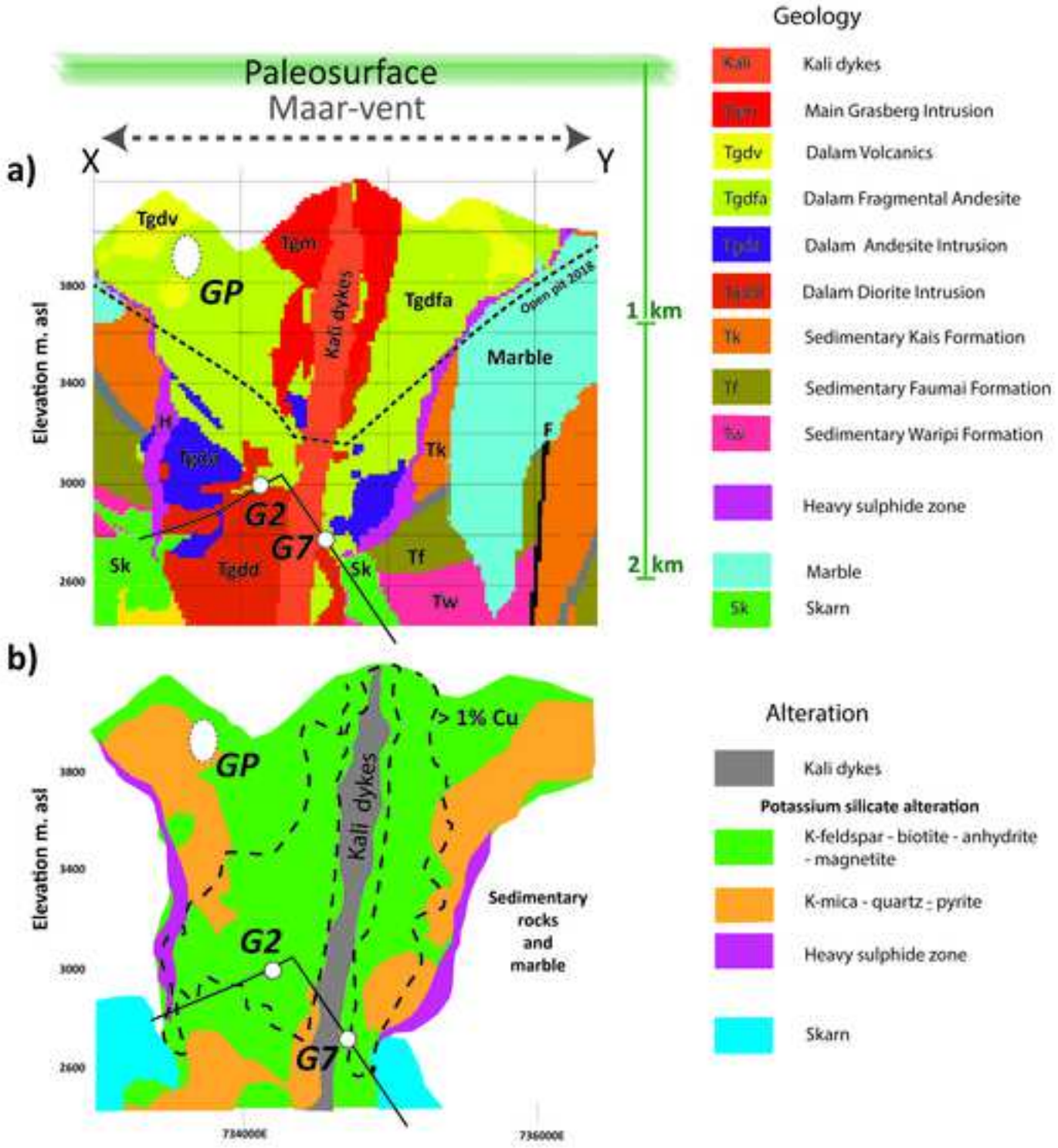

Figure

Click here to access/download;Figure;Figure 4 Rock samples.tif

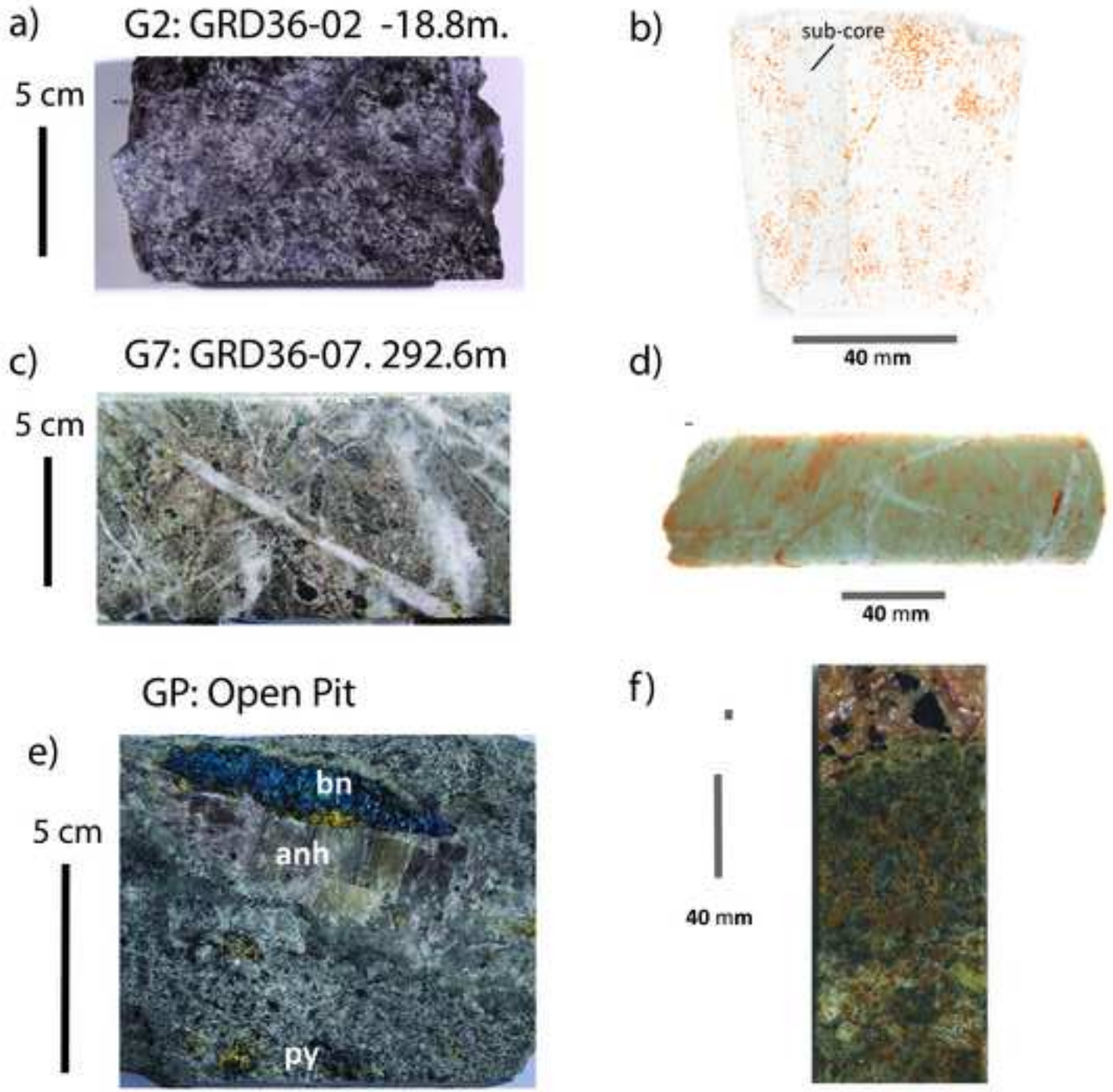

Figure

Click here to access/download;Figure;Figure 5 Dalam diorite section qem.tif

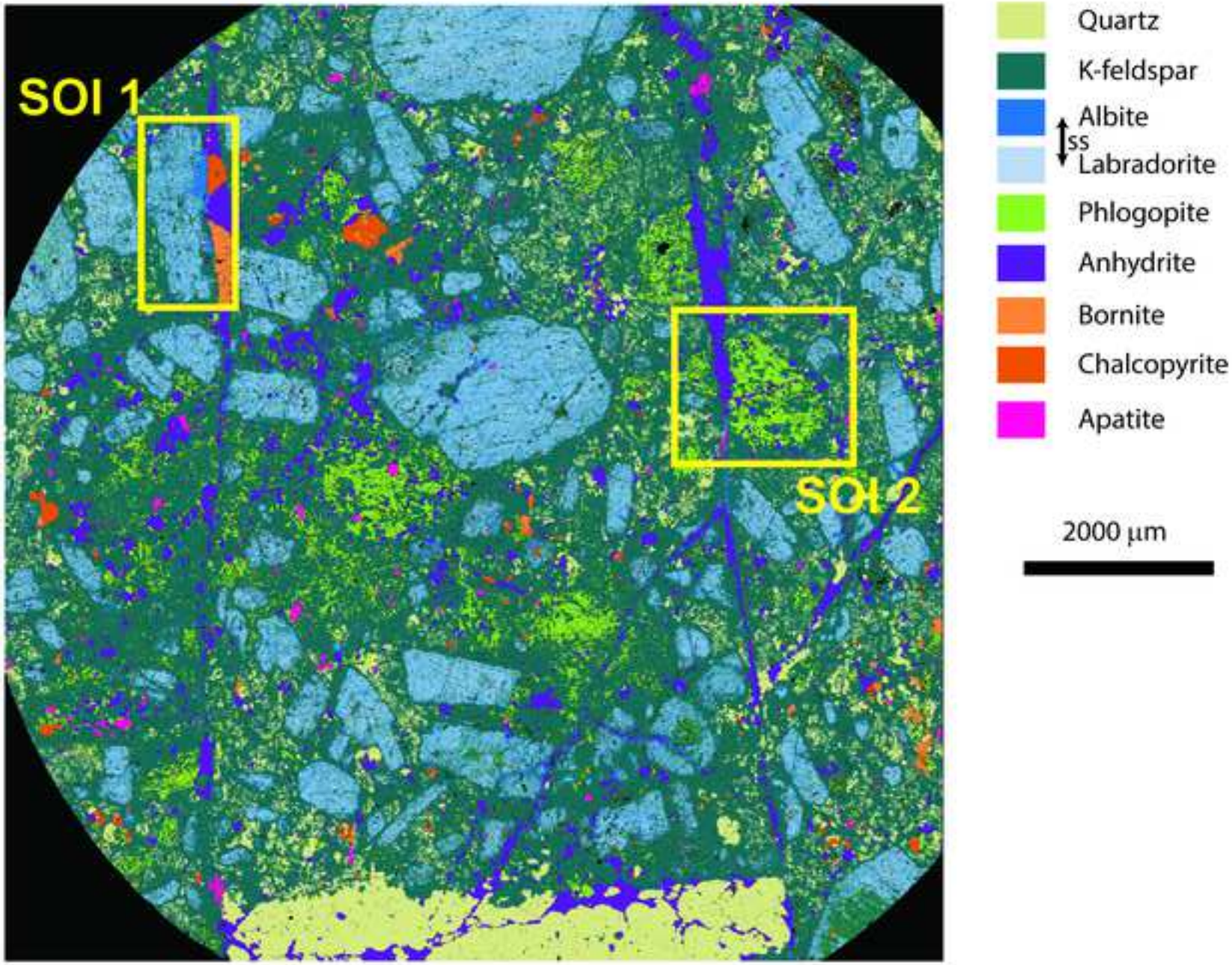

Figure

Click here to access/download;Figure;Figure 6 Labelled qem SOI1 .tif

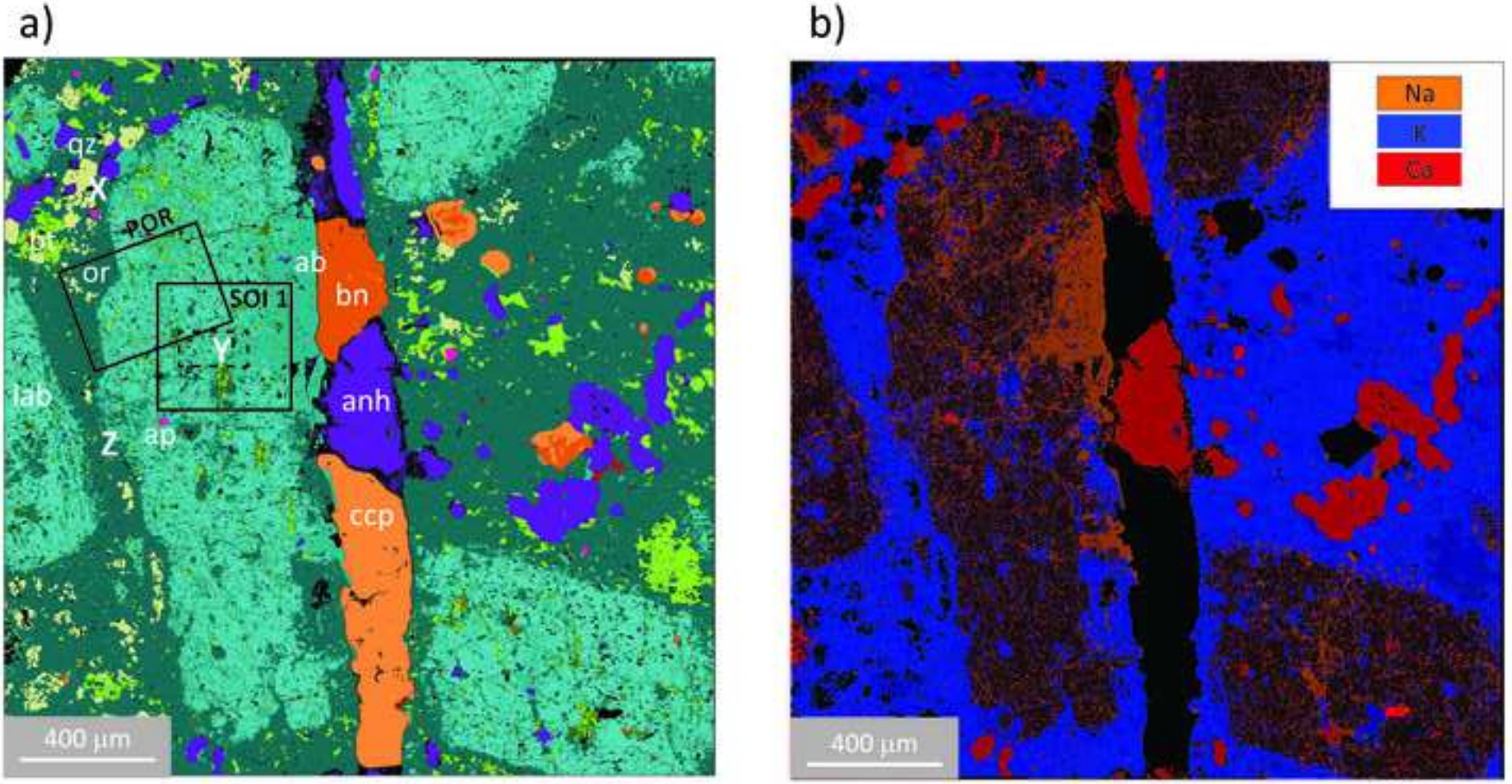

Figure

Click here to access/download;Figure;Figure 7 Feldspar ternary plot.tif

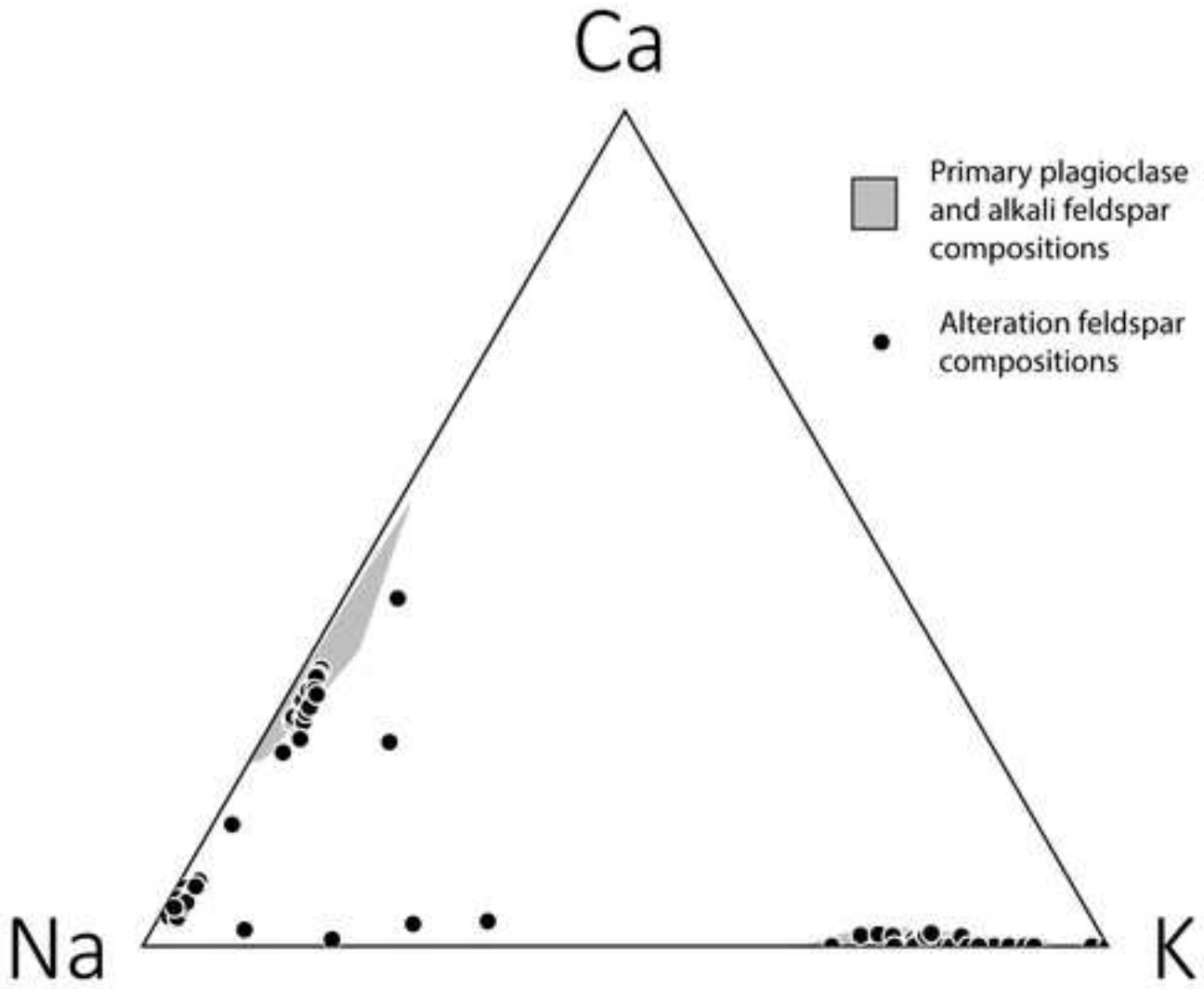

Figure

Click here to access/download;Figure;Figure 8 dalam biotite SOI2 qem high res.tif

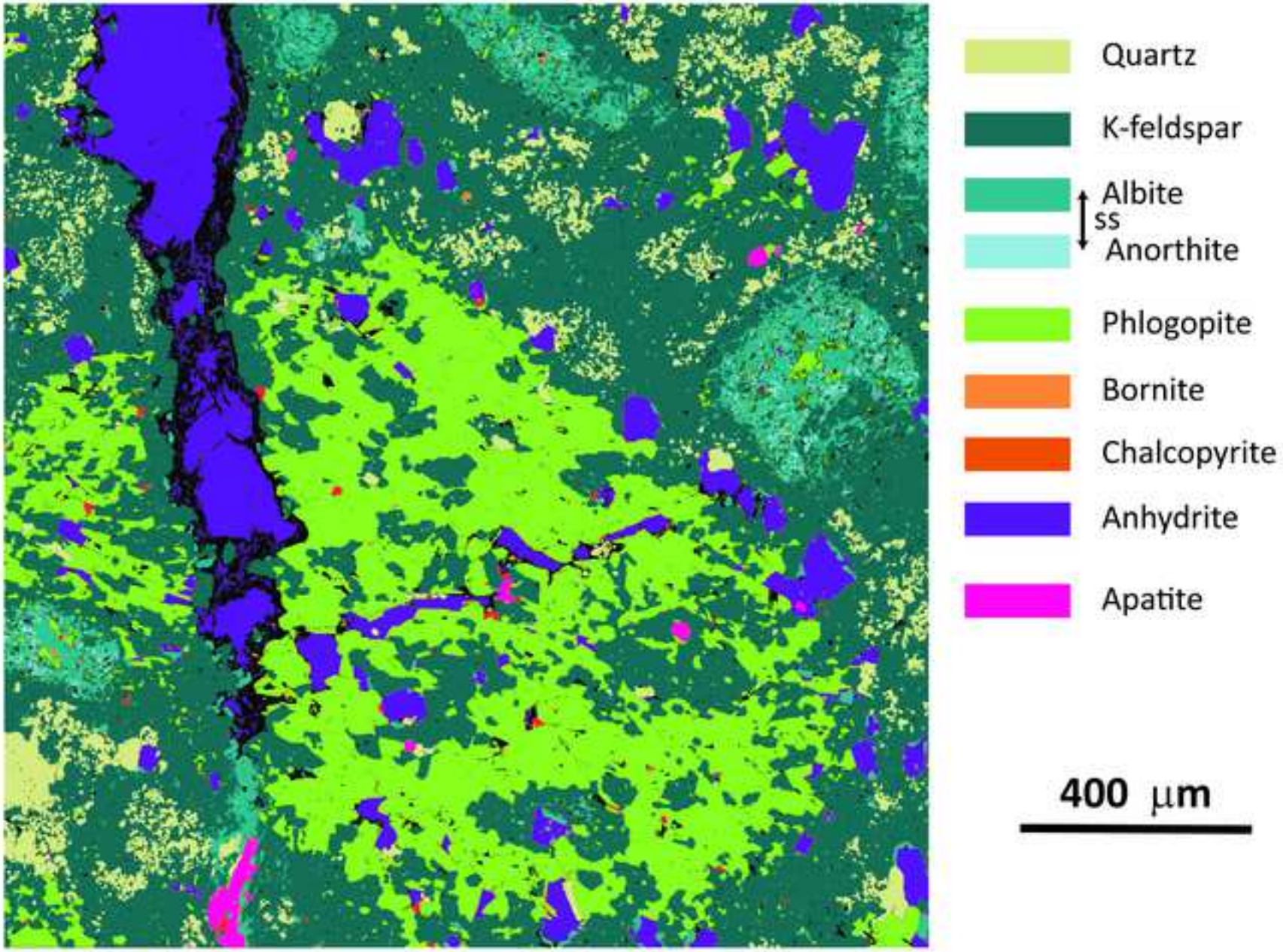

Figure

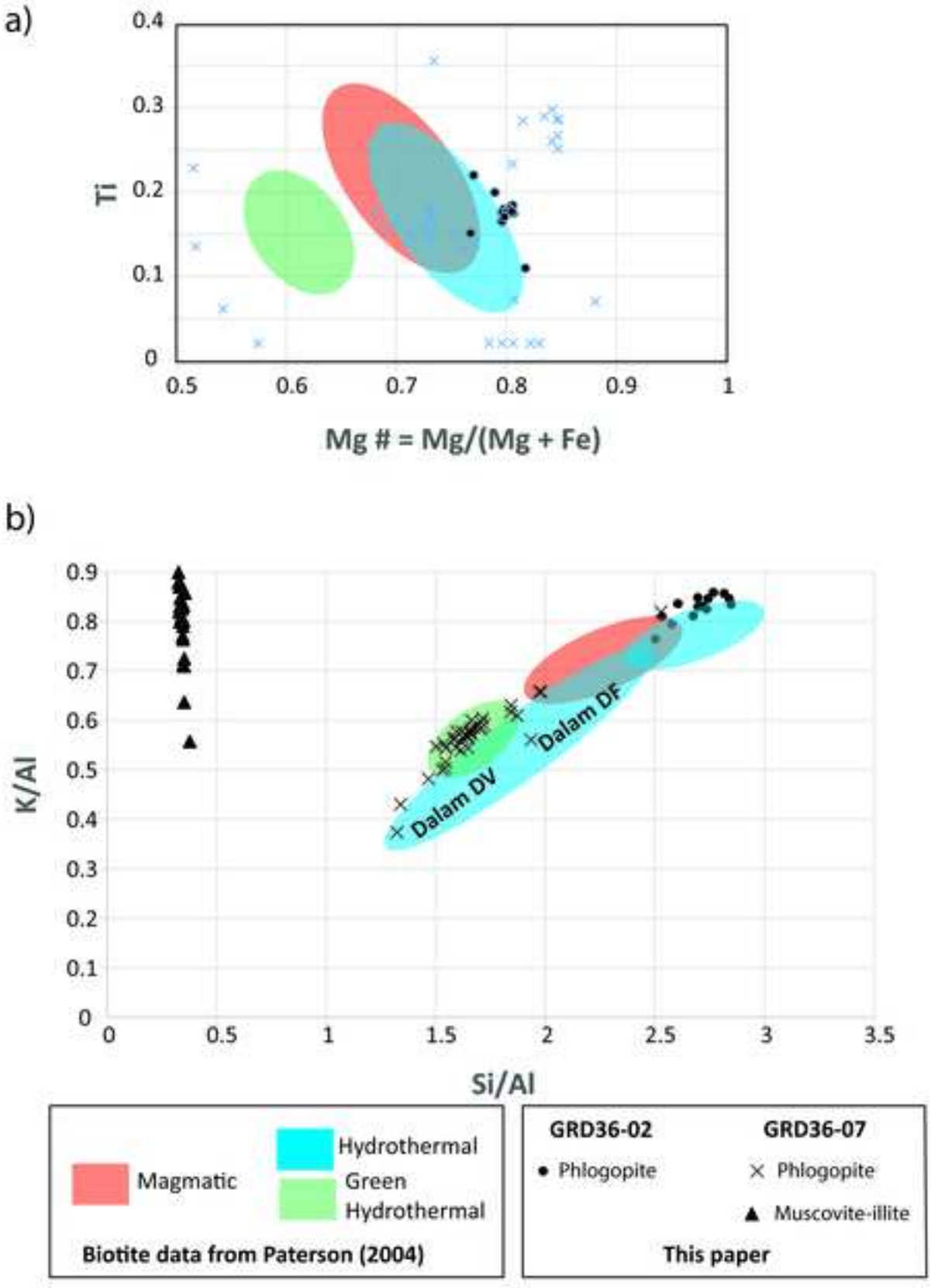

Figure

Click here to access/download;Figure;Figure 10 G7 RKO6 qem mineral map.tif

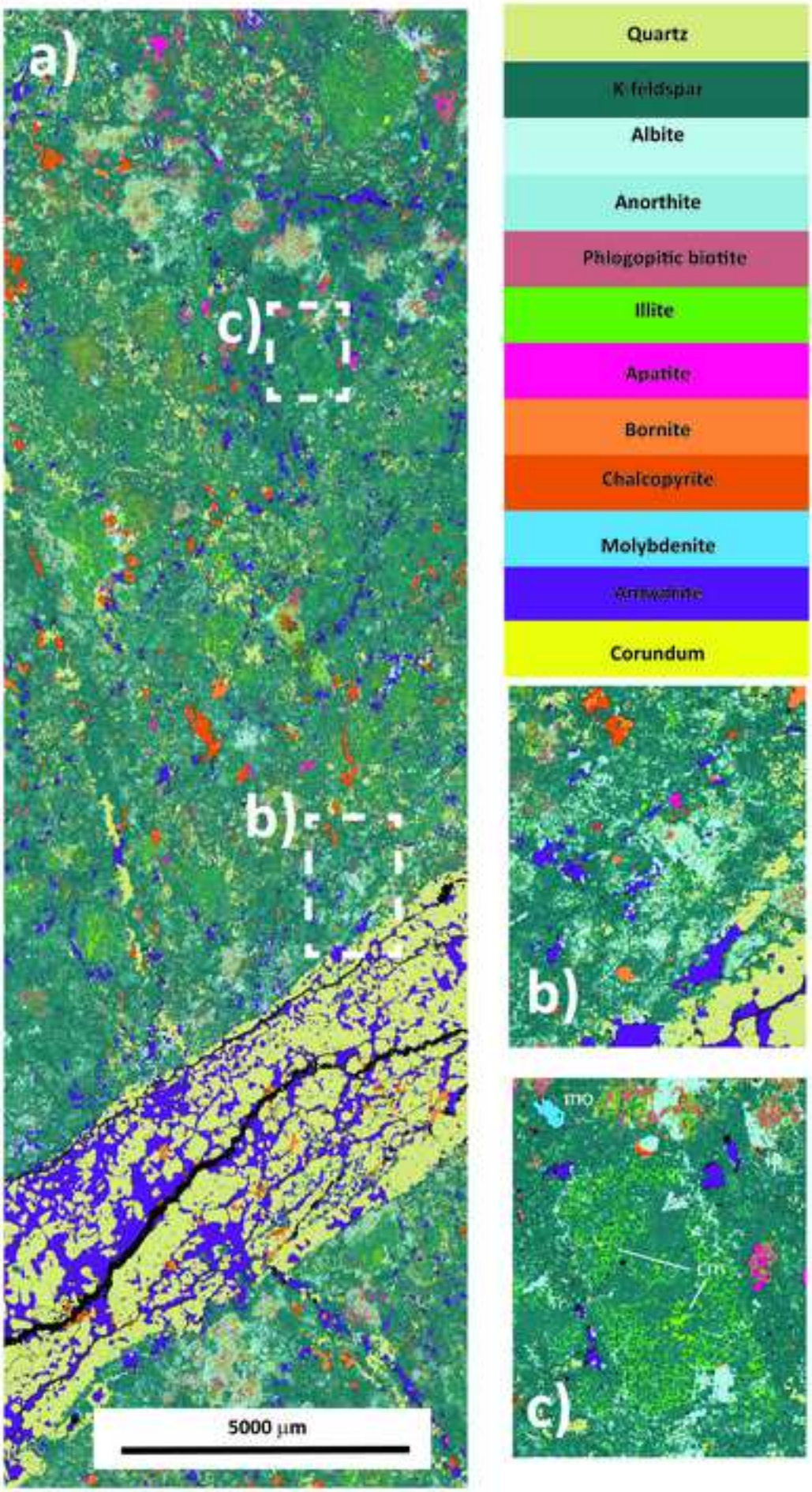

Figure

Click here to access/download;Figure;Figure 11 Open pit sample and qem map.tif

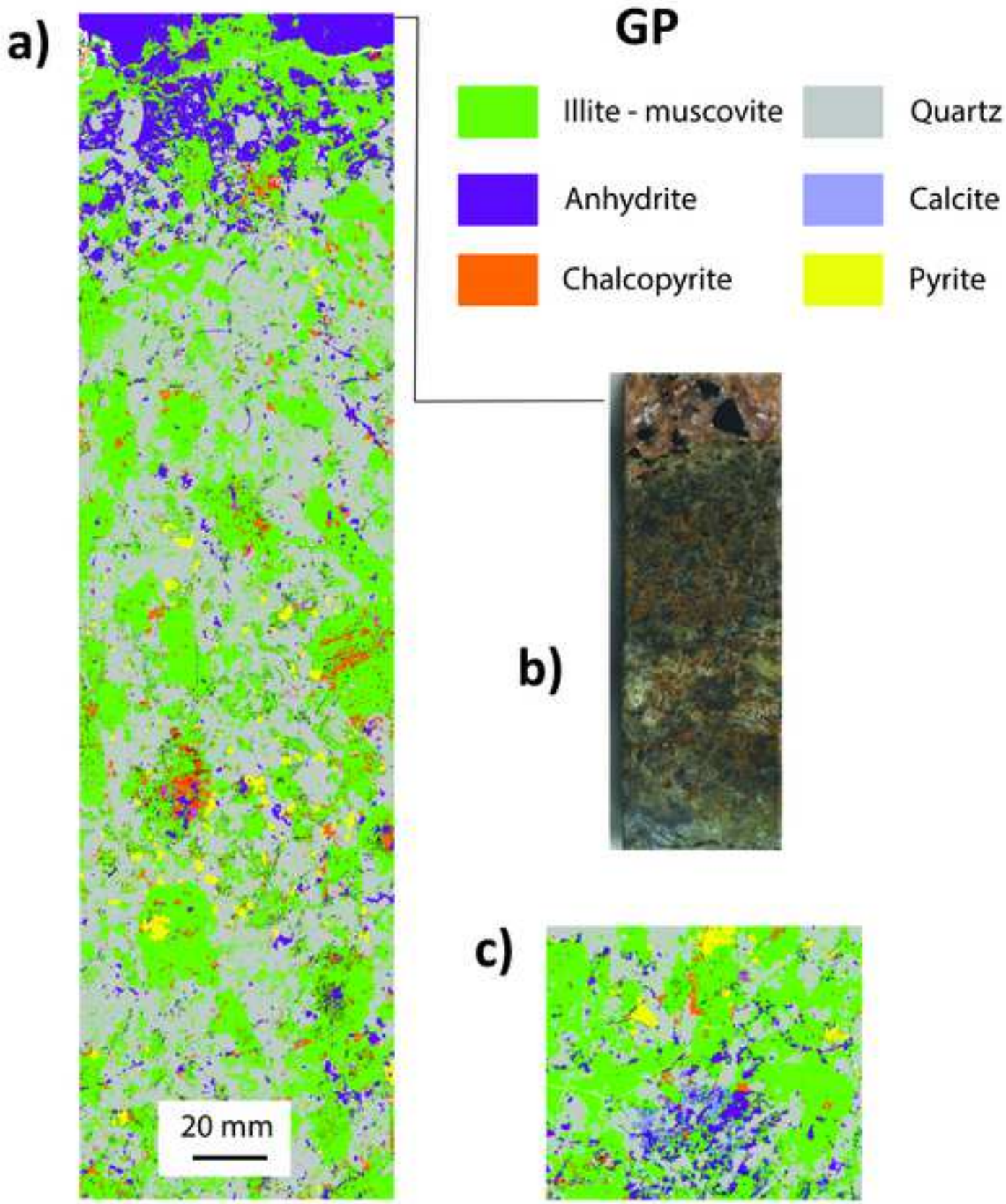

Figure

Click here to access/download;Figure;Figure 12 New Joe porosity (1).tif

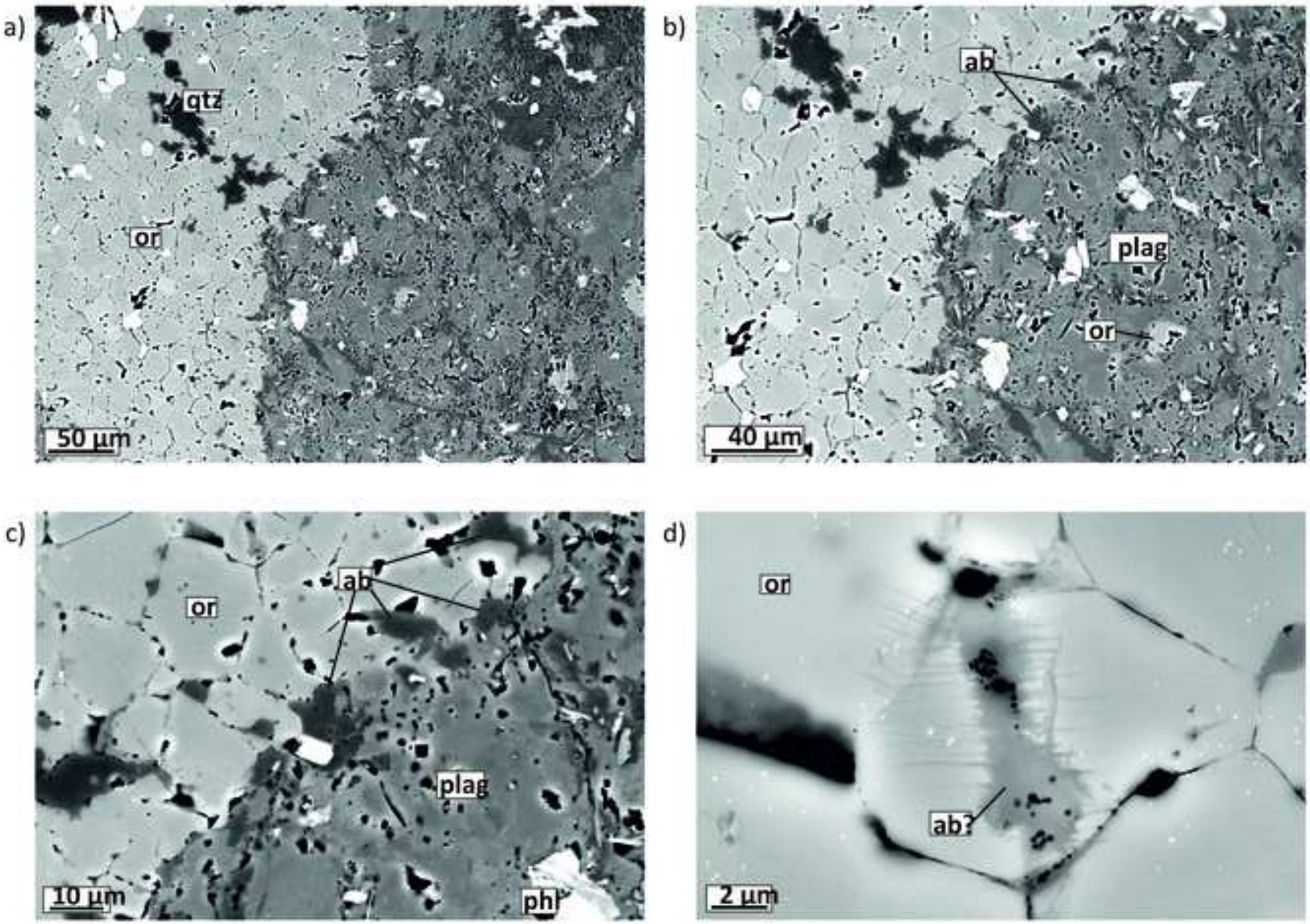

Figure

Click here to access/download;Figure;Figure 13 G2 porosity Yulai.tif

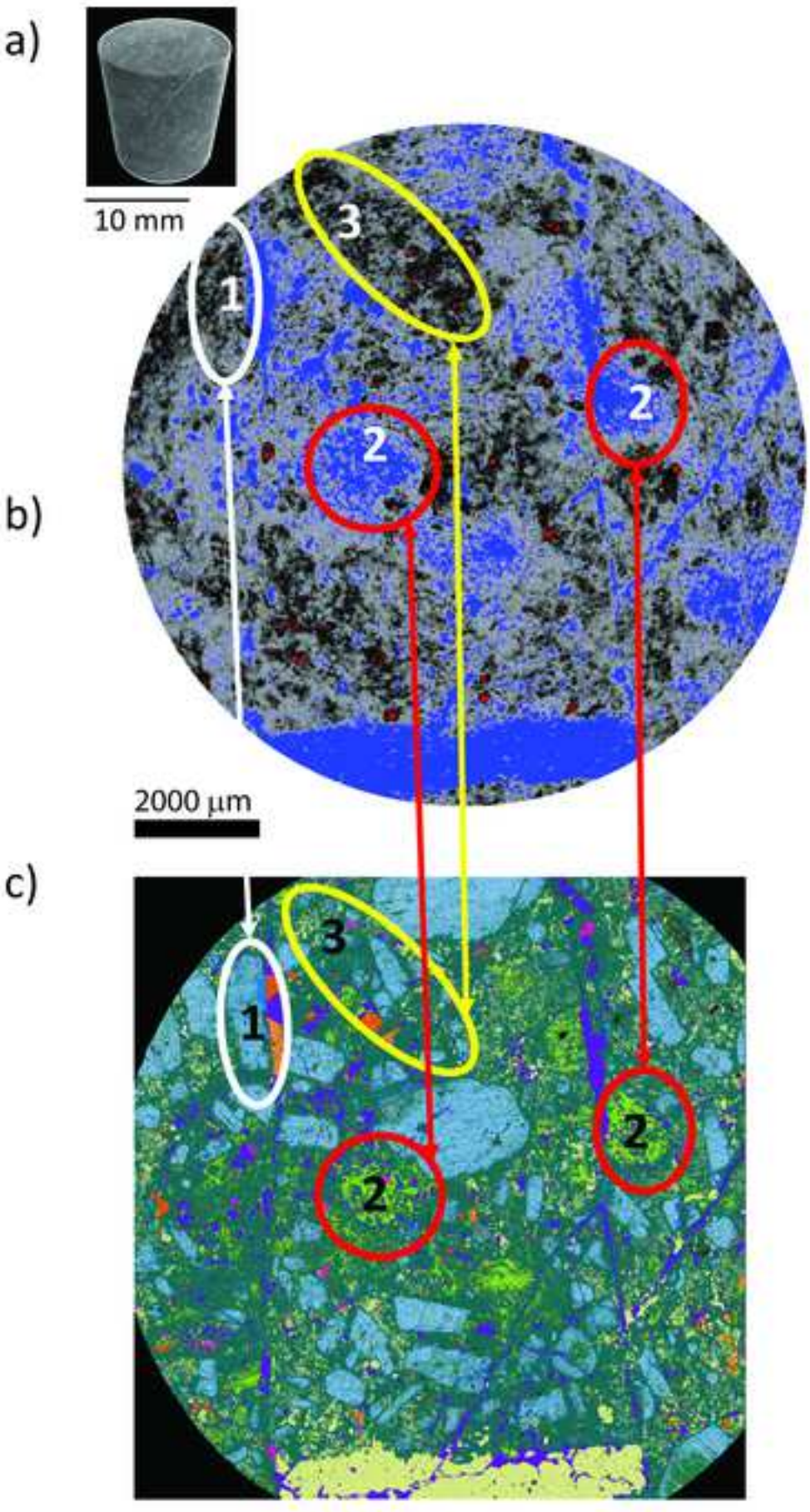

Figure

Click here to access/download;Figure;Figure 14 only G7 porosity.tif

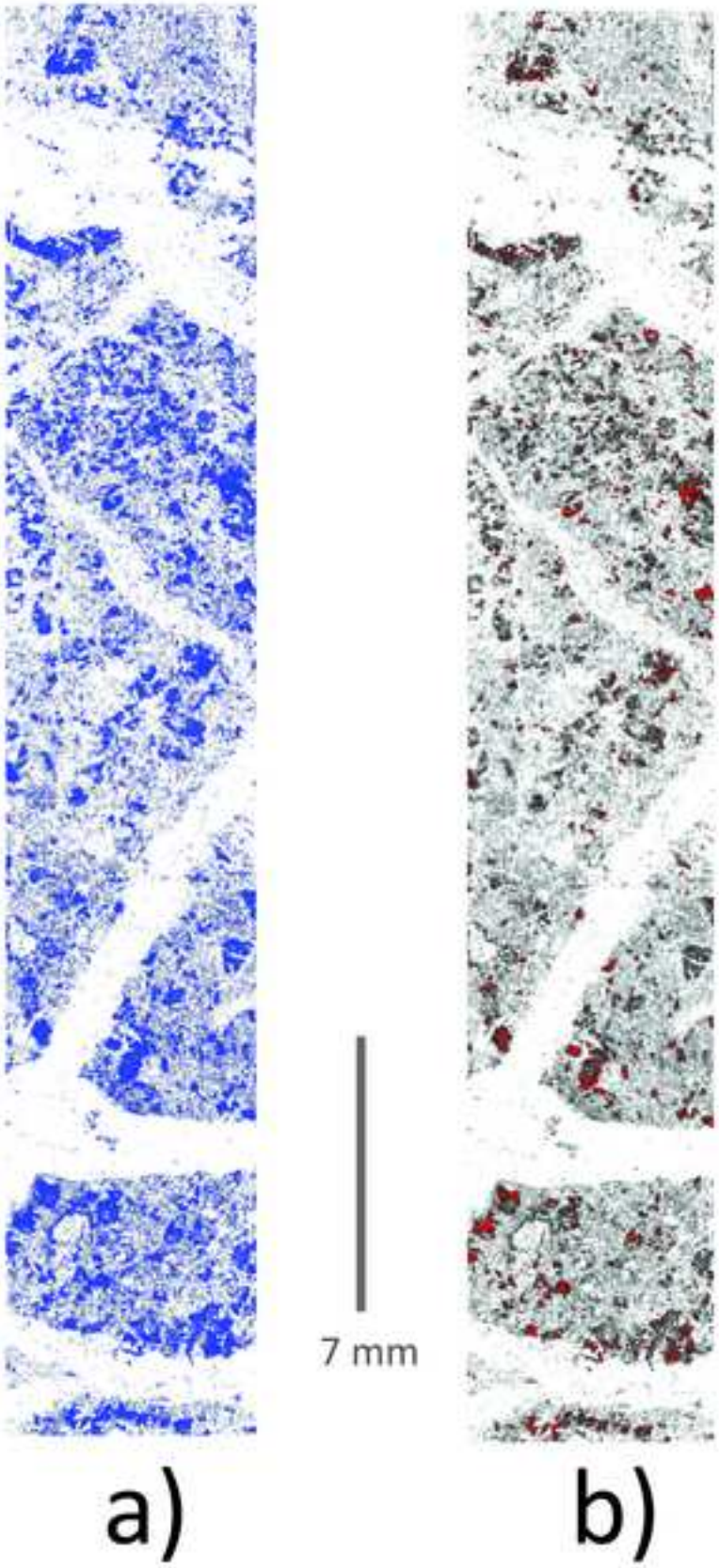

Figure

Click here to access/download;Figure;Figure 15 revised FI in anhydrite.tif

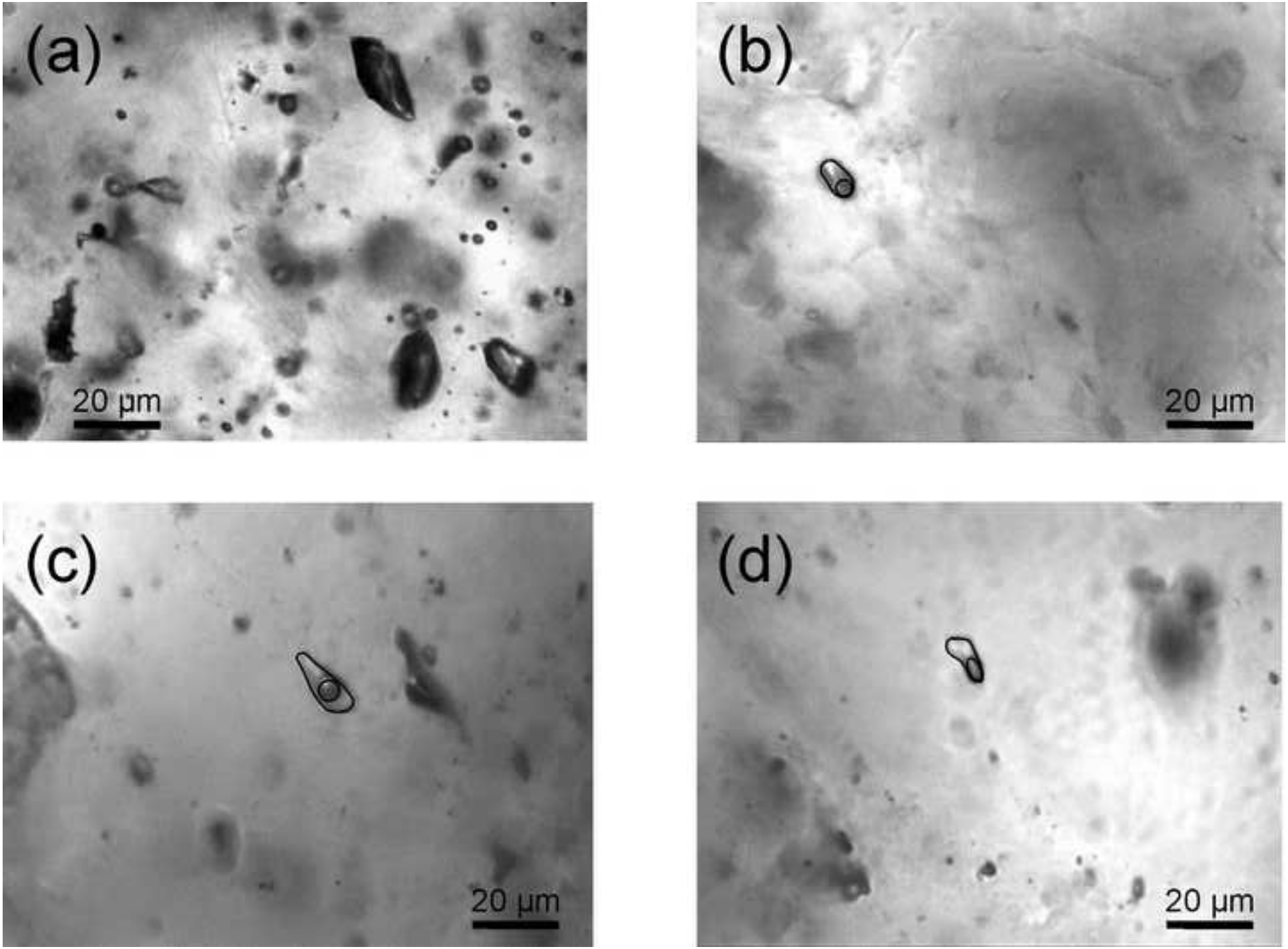

Figure

Click here to access/download;Figure;Figure 16 v2 maar volcano.tif

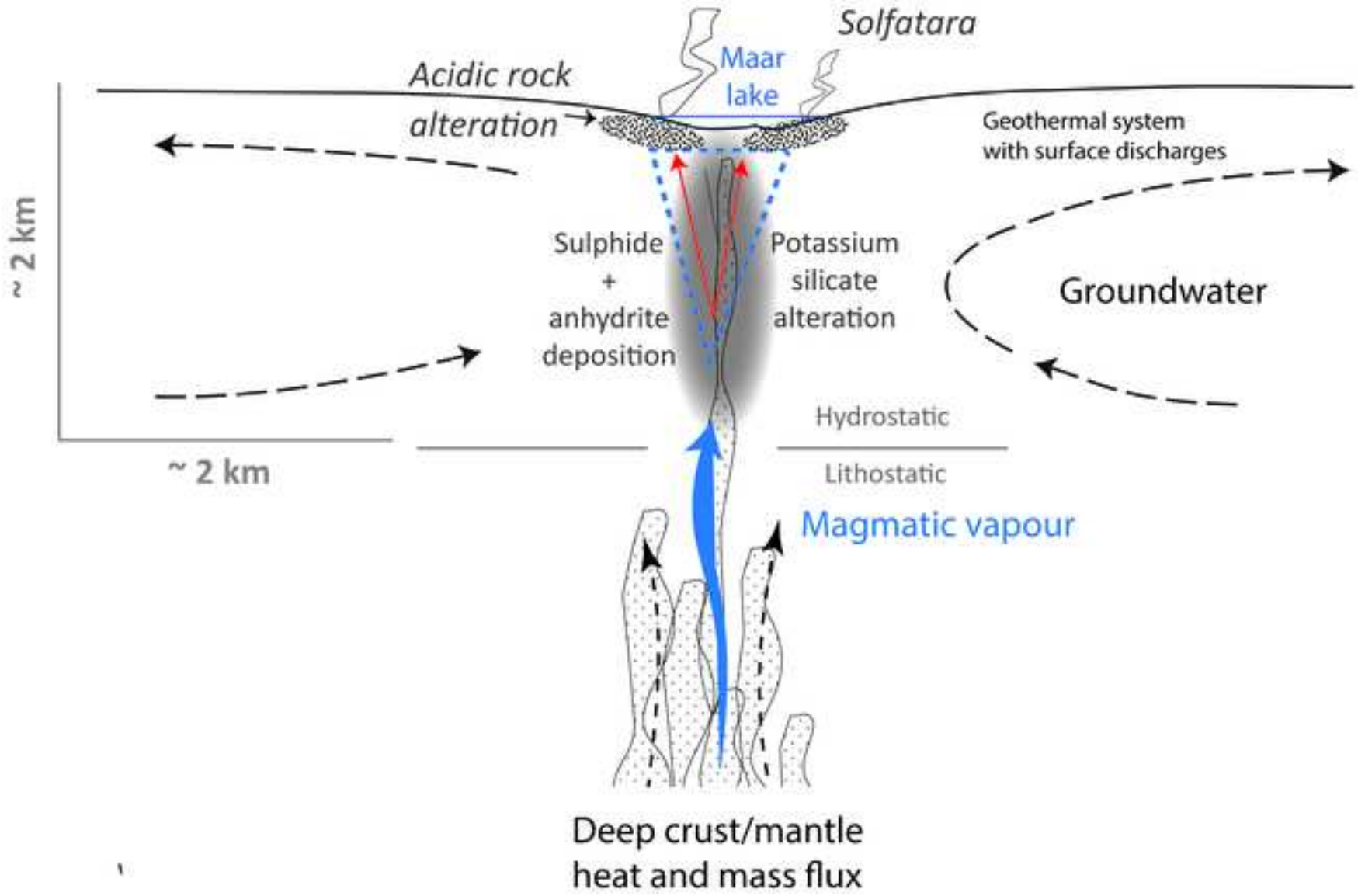

Figure

Click here to access/download;Figure;Figure 17 Mass balance-01.tif

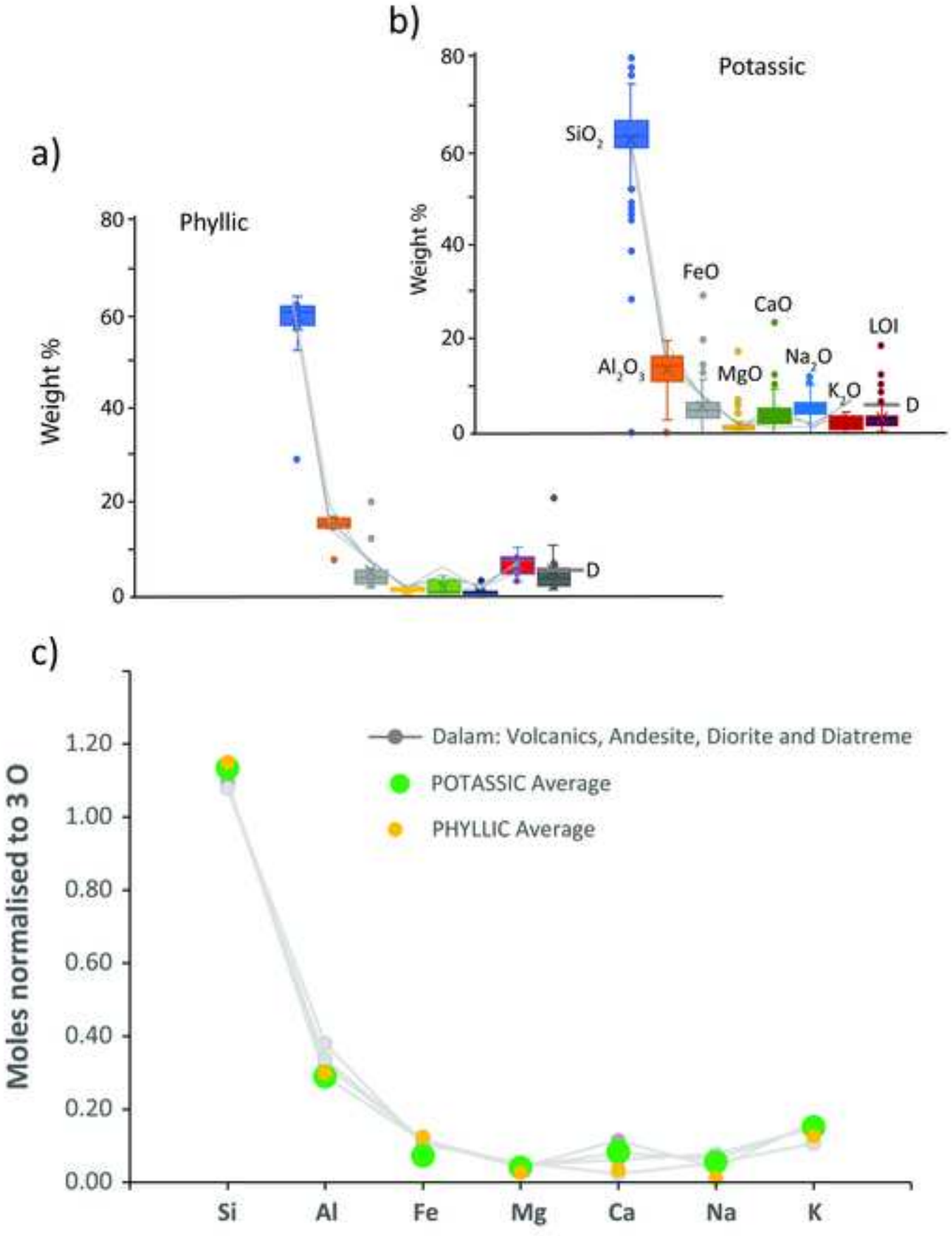

Figure

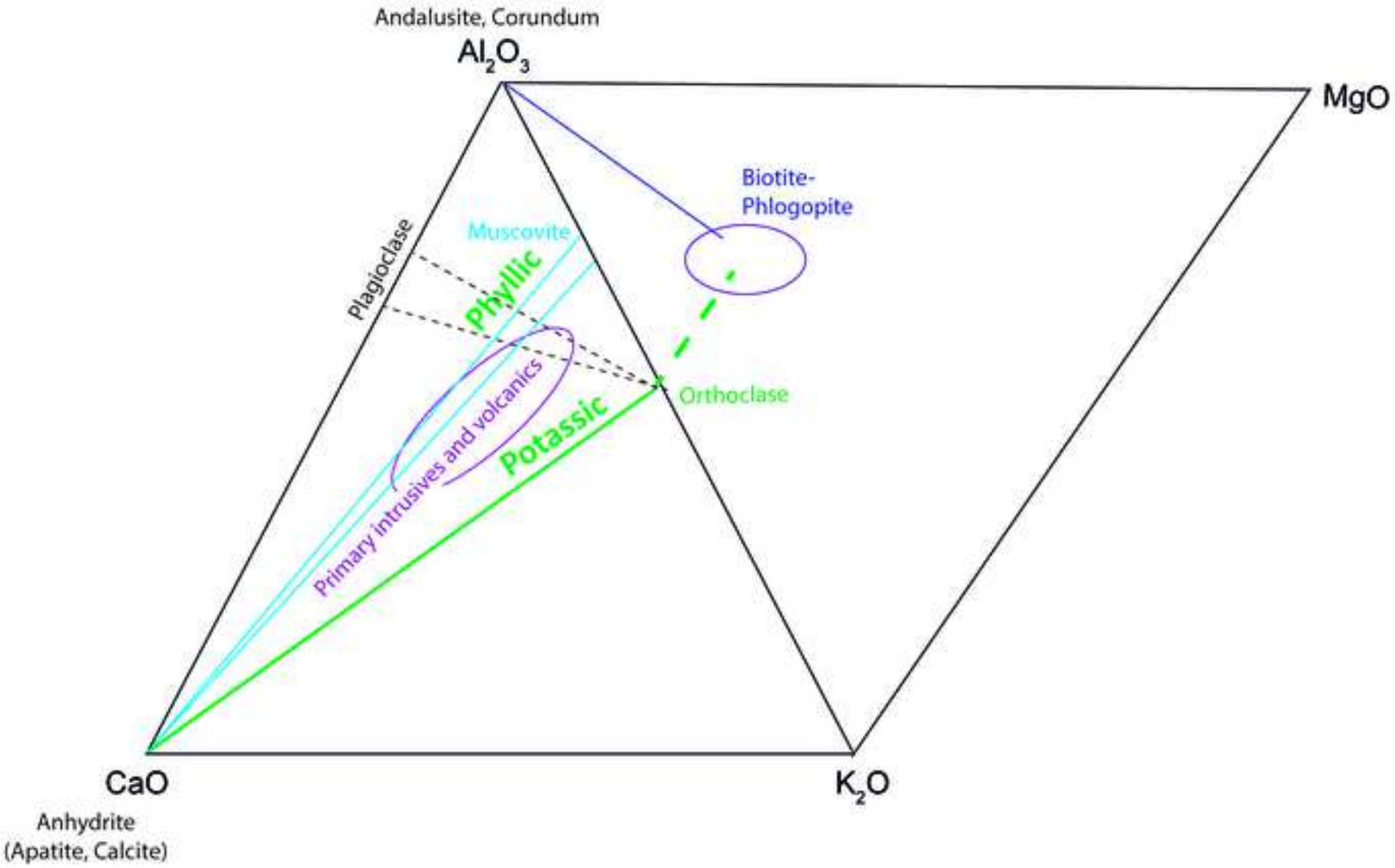

Figure

Click here to access/download;Figure;Figure 19 Contour adiabatic overlay plots.tif

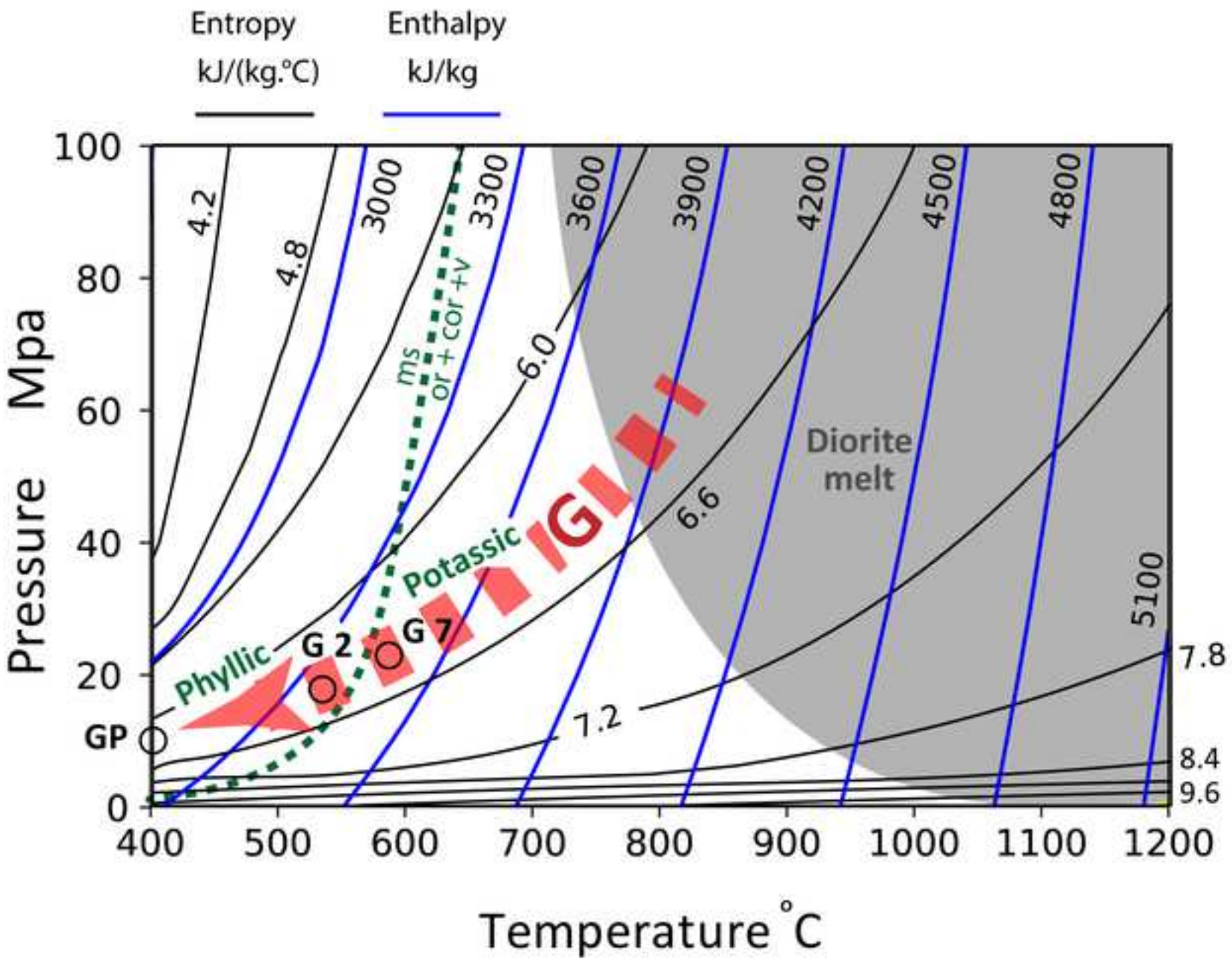

Figure

Click here to access/download;Figure;Figure 20 Element summary.tif

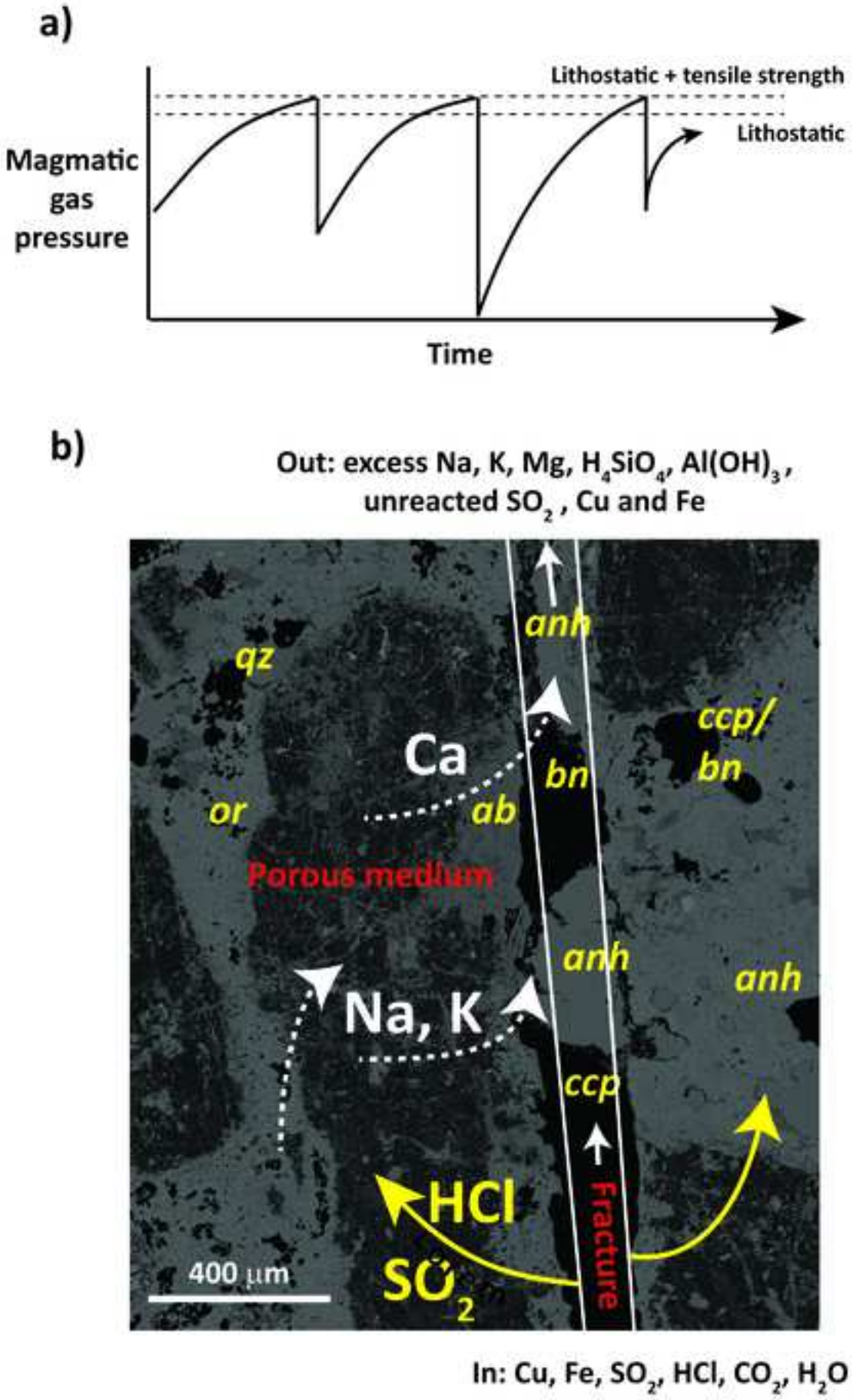

wt %	Dalam Volcanics	Dalam Diatreme	Dalam Diorite	Dalam Andesite
SiO_2	63.83	61.90	62.25	61.73
Al_2O_3	18.94	15.49	14.00	16.29
FeO	7.36	7.85	7.62	7.97
MgO	2.09	1.72	1.56	1.82
CaO	1.29	4.26	6.06	3.25
Na_2O	1.58	1.88	1.18	2.29
K_2O	4.91	6.89	7.33	6.65

Alteration Type	Potassic	Phyllic
Total volume m^3	1,052,750,250	1,168,114,500
No. of XRD samples	2,906	824
	Weight %	Weight %
Quartz	25	30
K Feldspar	30	11
Plagioclase	14	3
Muscovite	7	19
Biotite-Phlogopite	5.2	3.2
Anhydrite	4	1.8
Gypsum	3.7	1.8
Kaolinite	0.19	0.47
Swelling clay	1.4	2.2
Magnetite	0.71	0.58
Pyrite	1.9	14.3
Chalcopyrite	1.48	1.38
Bornite	0.33	0.06
Covellite	0.14	0.2
Amphibole	0.3	0.7
Pyroxene	0.2	0.7

Total wt %	95.05	88.99

Sample	Elevation[a]	Paleo-depth	Pl+ Θ	$P_{groundwater}$	T_S[c]	ρ_g
	m.a.s.l.	m.	MPa[b]	MPa	°C	$kg.m^{-3}$
G2:GRD36-02	3050	1450	40.1	14.2	535	42
G7:GRD36-07	2800	1700	46.9	16.7	565	48
GP: Open Pit	>3700	<800	<22.6	<7.8	<415	<24

. [a] Elevations are with respect to present day sea level.

[b] Maximum (Lithostatic + tensile strength) and minimum (groundwater) pressures at the estimated paleo-depths

c T_S is the equivalent temperature at maximum pressure along an isentropic expansion path. based on the model described in the text for S_{H2O} ~ 6.5 kJ/(kg.°C)

[d] ρ_g is the gas phase density at the pressures and temperatures along the isentropic expansion path taking water as the dominant component (>90 mole percent) of magmatic gas mixtures.

	G2	G7
K-feldspar	50.32%	51.99%
Quartz (Silica)	11.40%	14.76%
Labradorite solid solution	18.89%	
Anorthite solid solution	9.83%	2.14%
Albite	9.06%	11.50%
Gypsum + Anhydrite	6.10%	6.46%
Phlogopitic-biotite	5.92%	4.85%
Muscovite/Illite	1.69%	4.09%
Bornite	0.55%	0.71%
Chalcopyrite	0.50%	0.89%
Apatite	0.48%	0.30%
Corundum		0.60%

a)	Number of samples analysed	SiO_2	Al_2O_3	FeO	MgO	CaO	Na_2O	K_2O
					wt %			
Average Potassic	1450	65.58	14.20	5.02	1.57	4.48	1.66	6.88
Std Deviation		9.73	3.16	4.53	1.33	3.63	1.11	2.16
Average Phyllic	792	67.08	14.80	8.68	0.99	1.84	0.33	5.76
Std Deviation		`14.92	4.61	7.55	1.69	3.24	0.57	2.63

b)	Si	Al	Fe	Mg	Ca	Na	K
Moles per 3 moles O							
Potassic Average	1.13	0.29	0.07	0.04	0.08	0.06	0.15
Phyllic Average	1.15	0.30	0.12	0.03	0.03	0.01	0.13
Dalam Volcanics	1.09	0.38	0.10	0.05	0.02	0.05	0.11
Dalam Diatreme	1.09	0.32	0.12	0.04	0.08	0.06	0.15
Dalam Diorite	1.10	0.29	0.11	0.04	0.11	0.04	0.16
Dalam Andesite	1.08	0.34	0.12	0.05	0.06	0.08	0.15

Gas species	Mole %	Minerals	Mole %
H_2O	96.3	$CaAl_2Si_2O_8$	0.094
CO_2	1.61	$NaAlSi_3O_8$	0.047
SO_2	1.27	$KAlSi_3O_8$	0.094
HCl	0.2	Fe_3O_4	0.0094
HF	0.03		
H_2	0.58		

	Volume km3	Rock kg	S wt%	kg H2O	Phyllic H2O	total kg water	w/r
Phyllic	1.17	2.99E+12	6.94	8.85E+12	5.98E+10	8.91E+12	2.98
Potassic	1.05	2.69E+12	3.26	3.74E+12	5.39E+10	3.80E+12	1.41
Total	**2.22**	**5.68E+12**		**1.26E+13**		**1.27E+13**	**2.24***

None of the authors have any Conflicts of Interest to declare

No author statement is warranted